Additive Manufacturing 78 (2023) 103833

Contents lists available at ScienceDirect

Additive Manufacturing

journal homepage: www.elsevier.com/locate/addma

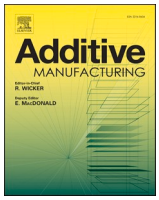

Topology optimisation for design and additive manufacturing of functionally graded lattice structures using derivative-aware machine learning algorithms

Chi Wu [a], Junjie Luo [b], Jingxiao Zhong [a], Yanan Xu [a], Boyang Wan [a], Wenwei Huang [a], Jianguang Fang [c], Grant P. Steven [a], Guangyong Sun [b], Qing Li [a,*]

[a] School of Aerospace, Mechanical and Mechatronic Engineering, The University of Sydney, Sydney, NSW 2006, Australia
[b] State Key Laboratory of Advanced Design and Manufacture for Vehicle Body, Hunan University, Changsha 410082, China
[c] School of Civil and Environmental Engineering, University of Technology Sydney, Sydney, NSW 2007, Australia

ARTICLE INFO

Keywords:
Topology optimisation
Derivative-aware machine learning
Functionally graded lattice structure
Additive manufacturing
Tissue scaffold

ABSTRACT

Although additive manufacturing has offered substantially new opportunities and flexibility for fabricating 3D complex lattice structures, effective design of such sophisticated structures with desired multifunctional characteristics remains a demanding task. To tackle this challenge, we develop an inventive multiscale topology optimisation approach for additively manufactured lattices by leveraging a derivative-aware machine learning algorithm. Our objective is to optimise non-uniform unit cells for achieving an as uniform strain pattern as possible. The proposed approach exhibits great potential for biomedical applications, such as implantable devices mitigating strain and stress shielding. To validate the effectiveness of our framework, we present two illustrative examples through the dedicated digital image correlation (DIC) tests on the optimised samples fabricated using a powder bed fusion (PBF) technique. Furthermore, we demonstrate a practical application of our approach through developing bone tissue scaffolds composed of optimised non-uniform iso-truss lattices for two typical musculoskeletal reconstruction cases. These optimised lattice-based scaffolds present a more uniform strain field in complex anatomical and physiological condition, thereby creating a favourable biomechanical environment for maximising bone formation effectively. The proposed approach is anticipated to make a significant step forward in design for additively manufactured multiscale lattice structures with desirable mechanical characteristics for a broad range of applications.

1. Introduction

Over the past two decades, topology optimisation has exhibited significant effectiveness and been found extensive applications in design of various lattice structures for a wide range of disciplines [1–5]. Nevertheless, the inherently high computational cost was ever a major bottleneck when handling complicated mono-scale models. To address this issue, a multiscale finite element (FE^2)-based framework has been developed to divide mono-scale design into macroscopic and microscopic optimisation problems [6]. Typically, a mono-scale lattice structure comprises periodically arranged unit cells, where homogenisation analyses can be carried out at a microscopic unit-cell level. The homogenised material properties are then used for FE analyses at a macroscopic level. Recently, machine learning (ML)-based techniques have drawn growing attention and undergone rapid development in design of lattice structures, which have exhibited compelling benefits and great potential in various engineering fields [7–12].

One of the emerging applications of topology optimisation for lattice structures is design of implantable devices in biomedical engineering, which involves rationally tailoring structural configurations of unit cells for surgical treatments [13–15]. Tissue scaffolds, used for treating critical size bone defects, are a typical example of such implants which have sophisticated porous architecture to facilitate cell attachment and tissue regeneration. Since additive manufacturing techniques demonstrate enormous potential to overcome the limitations to traditional fabrication of sophisticated 3D geometries, significant research efforts have been devoted to seeking tissue scaffolds composed of various complex geometries with desired biomechanical properties and physiological

* Corresponding author.
E-mail address: qing.li@sydney.edu.au (Q. Li).

https://doi.org/10.1016/j.addma.2023.103833
Received 17 May 2023; Received in revised form 7 August 2023; Accepted 14 October 2023
Available online 17 October 2023

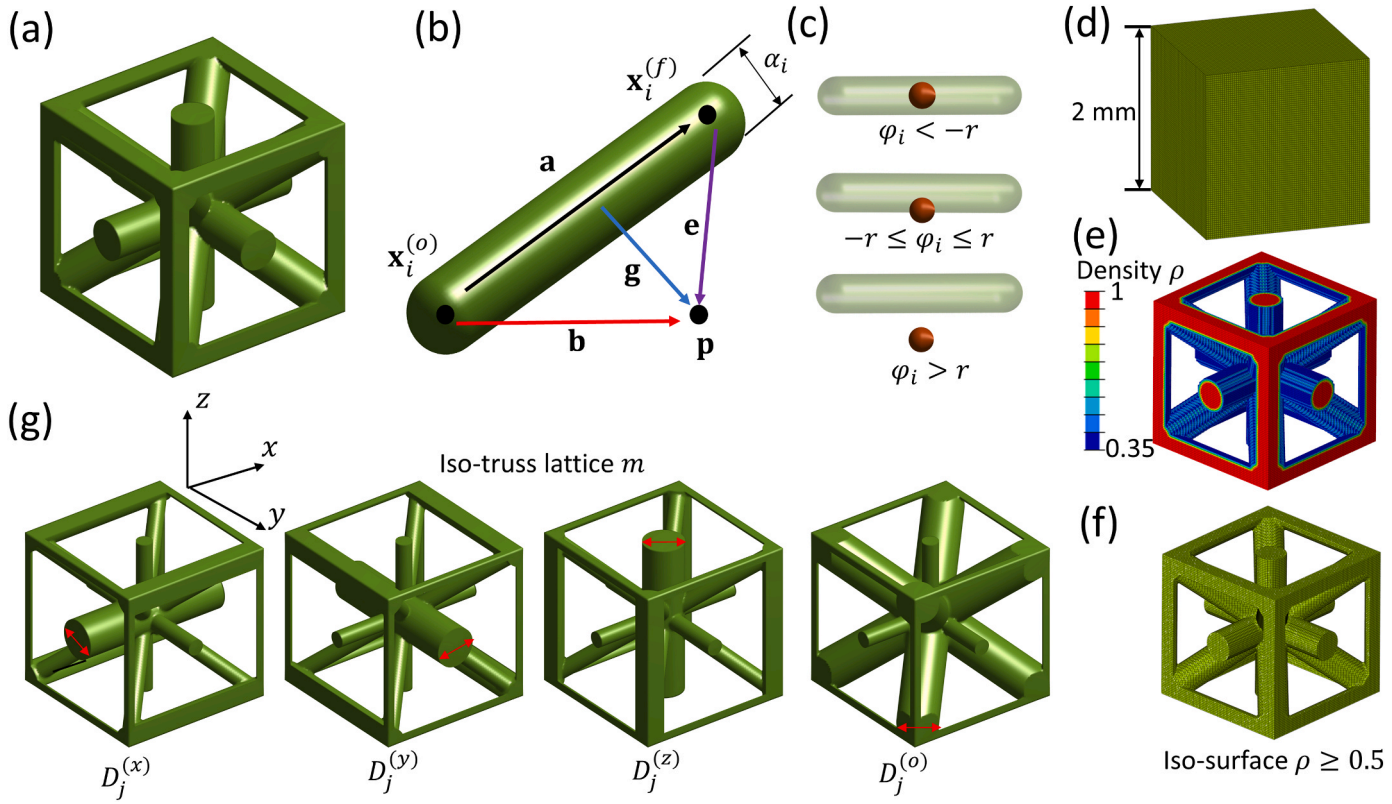

Fig. 1. Geometric projection of iso-truss lattices. (a) Geometry of iso-truss lattice structure. (b) The shortest distance of point **p** to bar *i* with a diameter α_i. Endpoints $\mathbf{x}_i^{(o)}$, $\mathbf{x}_i^{(f)}$ and $\mathbf{a}, \mathbf{b}, \mathbf{e}, \mathbf{g}$ are the vectors to determine the spatial location of **p** with respect to bar *i*. (c) A sphere to transform a discrete density to a continuous density ranging from 0 to 1. φ_i is a signed distance of **p** to bar *i*. The volume fraction of the sphere overlapped with bar *i* is defined as a continuous density of point **p**. (d) A FE model with an edge size of 2mm for homogenisation analyses, meshed with $80 \times 80 \times 80$ brick elements. (e) A reduced FE model after geometric projection and its density distribution. Elements with density 0 are excluded. The dark blue denotes the minimum density of 0.35, and the red colour represents the maximum density of 1. (f) An iso-surface model with density $\rho \ge 0.5$. (g) Design variables for the iso-truss lattice. $D_j^{(x)}, D_j^{(y)}, D_j^{(z)}$ and $D_j^{(o)}$ denote the diameters of bars towards x, y, z and diagonals directions, respectively.

functionalities [16–21]. Design of tissue scaffolds using trial-and-error approaches could be rather demanding when a large number of unit cells with different geometries need to be investigated [22]. Therefore, a more systematic approach with computational modelling and design optimisation techniques becomes appealing for fabricating new and high-performance tissue scaffolds [23].

Several well-established topology optimisation methods, such as the Solid Isotropic Material with Penalisation (SIMP) model [24], level-set representation [25,26], and bidirectional evolutionary structural optimisation (BESO) [27], etc., have been employed to design tissue scaffolds with maximum stiffness for bearing external loads [28]. Nevertheless, maximising the overall stiffness of bone scaffolds may not be ideal for promoting bone regeneration and could lead to strain shielding issues [29]. For this reason, designs with targeted stiffness have been suggested to overcome the stress/strain shielding issues by matching scaffold stiffness to host bone properties [14,30–32]. Nevertheless, tissue scaffolds composed of uniform unit cells would suffer from non-uniform strain patterns in a specific anatomical site, leading to some areas not meeting the proper strain thresholds required to support bone growth [33]. A number of *in-vivo* studies have shown that such non-uniform strain patterns would result in non-uniform bone formation [34,35]. To address this issue, additive manufacturing coupled with design optimisation for tailoring each unit-cell signifies a viable approach to achieving an as-possible uniform bone growth.

The integration of data-driven and ML-based techniques and additive manufacturing offers immense opportunities for design and fabrication of novel non-uniform lattices. Unfortunately, there is lack of study on such a design framework to develop novel lattice-based multiscale structures for potential applications in implantable devices. In order to fill this gap, we propose a derivative-aware ML optimisation approach here for design of lattice structures to achieve an as-possible uniform strain pattern toward a targeted strain. In this paper, two illustrative examples are first presented to demonstrate the effectiveness of the proposed design framework. The optimised lattice structures were fabricated by a powder bed fusion (PBF) technique, and the digital image correlation (DIC) tests were conducted to validate the as-possible strain patterns. Further, two musculoskeletal reconstruction cases were explored to optimise tissue scaffolds, thereby showing the ability of the proposed approach for real-life applications. The paper is anticipated to exhibit an effective framework to integrate ML in topology optimisation of functionally graded lattice structures for additive manufacturing.

2. Materials and methods

2.1. Problem definition

The objective is to achieve an as-possible uniform strain pattern by optimising the geometry of each unit cell in a design domain, which can be mathematically expressed as,

$$\begin{cases} \min\ (\varepsilon_V - \overline{\varepsilon}_V)^2 \\ \text{subject } to\ \mathbf{D}^{\mathrm{L}} \le \mathbf{D} \le \mathbf{D}^{\mathrm{U}} \end{cases}, \tag{1}$$

where ε_V represents an equivalent strain, expressed as [36,37],

$$\varepsilon_V = \frac{2}{3}\sqrt{\frac{(\varepsilon_{xx}-\varepsilon_{yy})^2+(\varepsilon_{xx}-\varepsilon_{zz})^2+(\varepsilon_{yy}-\varepsilon_{zz})^2}{2}+\frac{3\left(\gamma_{xy}^2+\gamma_{yz}^2+\gamma_{xz}^2\right)}{4}}, \tag{2}$$

in which $\varepsilon_{xx}, \varepsilon_{yy}$ and ε_{zz} are the engineering normal strains, and γ_{xy}, γ_{yz}, γ_{xz} are the engineering shear strains in 3D cases. In biomedical field, the equivalent strain ε_V provides an overall measure of strain on musculoskeletal tissue governing its mechanobiological responses [34,35]. By minimising the square error between ε_V and a targeted strain $\overline{\varepsilon}_V$, one can thus achieve an as-possible uniform equivalent strain pattern. $\mathbf{D}$, $\mathbf{D}^{\mathrm{L}}$ and $\mathbf{D}^{\mathrm{U}}$ denote the vectors of design variables and their lower and upper bounds to be depicted in the following section.

2.2. Geometric projection technique for unit cells

In this study, an iso-truss lattice (Fig. 1(a)) is chosen as a basic configuration of the unit cell for optimisation. The iso-truss lattice comprises 19 bars, with five bars towards each x, y, z directions and four bars towards diagonal directions, as illustrated in Fig. 1(a). The iso-truss lattice can be parameterised by a geometric projection technique [38,39], which is briefly depicted here.

Considering an arbitrary bar $i \in [1, 19]$ in the iso-truss lattice, its geometry can be intrinsically defined by the two endpoints $\mathbf{x}_i^{(o)}$, $\mathbf{x}_i^{(f)}$ and its diameter α_i (Fig. 1(b)). A signed distance φ_i describes the location of an arbitrary point $\mathbf{p}$ (Fig. 1(b)) to bar i as,

$$\varphi_i(\omega_i, \alpha_i) = \omega_i\left(\mathbf{x}_i^{(o)}, \mathbf{x}_i^{(f)}, \mathbf{p}\right) - \frac{\alpha_i}{2}, \tag{3}$$

where ω_i is the shortest distance from point $\mathbf{p}$ to bar i, calculated as,

$$\omega_i\left(\mathrm{x}_i^{(o)}, \mathrm{x}_i^{(f)}, \mathrm{p}\right) = \begin{cases} ||\mathrm{b}||, \mathrm{a}\bullet\mathrm{b} \le 0 \\ ||\mathrm{g}||, 0 < \mathrm{a}\bullet\mathrm{b} \le \mathrm{a}\bullet\mathrm{a} \\ ||\mathrm{e}||, \mathrm{a}\bullet\mathrm{b} > \mathrm{a}\bullet\mathrm{a} \end{cases}, \tag{4}$$

in which $\mathbf{a}, \mathbf{b}, \mathbf{g}, \mathbf{e}$ are the vectors as illustrated in Fig. 1(b), defined as,

$$\mathbf{a} = \mathbf{x}_i^{(f)} - \mathbf{x}_i^{(o)}, \tag{5}$$

$$\mathbf{b} = \mathbf{p} - \mathbf{x}_i^{(o)}, \tag{6}$$

$$\mathbf{e} = \mathbf{p} - \mathbf{x}_i^{(f)}, \tag{7}$$

$$\mathbf{g} = \left(\mathbf{I} - \frac{\mathbf{a}\otimes\mathbf{a}}{\mathbf{a}\bullet\mathbf{a}}\right)\bullet\mathbf{b}, \tag{8}$$

where $\mathbf{I}$ denotes the second-order identity, $\otimes$ is the outer product operator.

According to the signed distance φ_i defined in Eq. (3), point $\mathbf{p}$ lies in bar i if $\varphi_i \le 0$, while point $\mathbf{p}$ is outside bar i if $\varphi_i > 0$. Therefore, a discrete density value $\chi = 1$ or 0 can be employed to denote point $\mathbf{p}$ inside or outside bar i, respectively. As χ is discrete and non-differentiable, a spherical region (Fig. 1(c)) with radius $r \ll \alpha_i$ is employed to enable a continuous density $\overline{\rho}_i$ ranging from 0 to 1 [39], given as,

$$\overline{\rho}_i = \begin{cases} 1, \varphi_i < -r \\ \dfrac{(r-\varphi_i)^2(2r+\varphi_i)}{4r^3}, -r \le \varphi_i \le r \\ 0, \varphi_i > r \end{cases}. \tag{9}$$

In order to consider the density ρ_p of point $\mathbf{p}$ corresponding to all the 19 bars in the iso-truss lattice, a η-norm function is adopted to determine ρ_p, namely the maximum density of point $\mathbf{p}$ among $\{\overline{\rho}_i |\ i = 1, 2, 3, \ldots, 19\}$, expressed as,

$$\rho_p = \left(\sum_{i=1}^{19} \overline{\rho}_i^{\eta}\right)^{\frac{1}{\eta}}. \tag{10}$$

When $\eta \to \infty$, Eq. (10) takes the maximum $\overline{\rho}_i$ for ρ_p. In this study, η is chosen as 30 to preserve the differentiability [38]. Using ρ_p, the material properties at point $\mathbf{p}$ can be interpolated as,

$$\mathbf{C}_p = \rho_p \mathbf{C}_{base}, \tag{11}$$

where $\mathbf{C}_p$ is the elastic tensor at point $\mathbf{p}$, $\mathbf{C}_{base}$ denotes the elastic tensor of base materials with linear elastic isotropic properties.

Without loss of generality, a cubic unit-cell with an edge size of 2 mm is considered here to model the parameterised iso-truss lattice. The unit-cell is meshed by $80 \times 80 \times 80$ brick elements (Fig. 1(d)) with full integration. The centroids of brick elements are used to project the iso-truss lattice, in which the elements with densities $\rho_p = 0$ are excluded from the full FE model to lower the computational cost. Fig. 1(e) shows a reduced FE model and the density distribution, in which the diameters of the bars are 0.4 mm. Fig. 1(f) plots an iso-surface of $\rho_p \ge 0.5$, demonstrating the consistency of the geometric projection in the FE model.

Intrinsically, the geometric projection method enables us to control the diameter of every single bar in an iso-truss lattice, as shown in Supplementary Movie 1. To simplify the optimisation problem, the diameters of the bars towards x, y, z and diagonal directions are chosen as the design variables $\mathbf{D} = \left\{D_j^{(x)}, D_j^{(y)}, D_j^{(z)}, D_j^{(o)}\right\}$, respectively, as outlined in Fig. 1(g), where $j \in [1, J]$ and J denotes the total number of iso-truss lattices in design domains.

Supplementary material related to this article can be found online at doi:10.1016/j.colsurfa.2023.132032.

2.3. Sensitivity analysis

A multiscale finite element (FE^2) method is adopted here to reduce the computational cost of the design problem as defined in Eq. (1). At the macroscopic level, a design model is discretised by macro brick elements without the geometrical details of the iso-truss lattices. At the microscopic level, the elastic tensors of each macro brick element are calculated using an asymptotic homogenisation technique [40]. First, we need to derive the sensitivity at the macroscopic level. Eq. (1) can be rewritten in its FE form as,

$$\begin{cases} \min \mathscr{L} = \sum_{j=1}^{J}\sum_{\xi=1}^{\aleph}\left(\epsilon_V^{(\xi j)} - \overline{\varepsilon}_V\right)^2 \\ \text{subject to } \mathrm{KU} = \mathrm{F} \\ \mathrm{D}^{\mathrm{L}} \le \mathrm{D}_j \le \mathrm{D}^{\mathrm{U}} \end{cases} \tag{12}$$

where each macro brick element j corresponds to an iso-truss lattice unit-cell j with the design variables $(\mathbf{D}_j = D_j^{(x)}, D_j^{(y)}, D_j^{(z)}, D_j^{(o)})$ as defined previously. ξ and $\aleph$ denote the integration points and the total number of integration points in macro element j, respectively. $\mathbf{K}$, $\mathbf{U}$, and $\mathbf{F}$ are the global stiffness matrix, global displacement vector, and global force vector at the macroscopic level, respectively.

The sensitivity of the design objective $\mathscr{L}$ with respect to $\mathbf{D}_j$ can be calculated as,

$$\frac{\mathrm{d}\mathscr{L}}{\mathrm{d}\mathbf{D}_j} = \sum_{j=1}^{J}\sum_{\xi}^{\aleph} 2\left(\varepsilon_V^{(\xi j)} - \overline{\varepsilon}_V\right)\frac{\mathrm{d}\varepsilon_V^{(\xi j)}}{\mathrm{d}\mathbf{D}_j}, \tag{13}$$

where the sensitivity of $\varepsilon_V^{(\xi j)}$ with respect to $\mathbf{D}_j$ is deduced as,

$$\frac{\mathrm{d}\varepsilon_V^{(\xi j)}}{\mathrm{d}\mathbf{D}_j} = \frac{\mathrm{d}\varepsilon_V^{(\xi j)}}{\mathrm{d}\boldsymbol{\varepsilon}^{(\xi j)}}\frac{\mathrm{d}\boldsymbol{\varepsilon}^{(\xi j)}}{\mathrm{d}\mathbf{D}_j}, \tag{14}$$

where $\boldsymbol{\varepsilon}^{(\xi j)}$ denotes the Cauchy strain tensor at integration point ξ in

macro element j. $\varepsilon_V^{(\xi j)}$ can be expressed in terms of $\boldsymbol{\varepsilon}^{(\xi j)}$ as,

$$\varepsilon_V^{(\xi j)} = \left[\frac{4}{9}\left(\boldsymbol{\varepsilon}^{(\xi j)}\right)^{\mathrm{T}}\mathbf{V}\boldsymbol{\varepsilon}^{(\xi j)}\right]^{\frac{1}{2}}, \tag{15}$$

$$\mathbf{V} = \begin{bmatrix} 1 & -0.5 & -0.5 & 0 & 0 & 0 \\ -0.5 & 1 & -0.5 & 0 & 0 & 0 \\ -0.5 & -0.5 & 1 & 0 & 0 & 0 \\ 0 & 0 & 0 & 0.75 & 0 & 0 \\ 0 & 0 & 0 & 0 & 0.75 & 0 \\ 0 & 0 & 0 & 0 & 0 & 0.75 \end{bmatrix}. \tag{16}$$

By substituting Eq. (15) into Eq. (14), one can have,

$$\frac{\mathrm{d}\varepsilon_V^{(\xi j)}}{\mathrm{d}\mathbf{D}_j} = \frac{2}{3}\frac{1}{2}\left[\left(\boldsymbol{\varepsilon}^{(\xi j)}\right)^{\mathrm{T}}\mathbf{V}\boldsymbol{\varepsilon}^{(\xi j)}\right]^{\frac{-1}{2}} 2\left(\boldsymbol{\varepsilon}^{(\xi j)}\right)^{\mathrm{T}}\mathbf{V}\frac{\mathrm{d}\boldsymbol{\varepsilon}^{(\xi j)}}{\mathrm{d}\mathbf{D}_j}, \tag{17}$$

which can be simplified as,

$$\frac{\mathrm{d}\varepsilon_V^{(\xi j)}}{\mathrm{d}\mathbf{D}_j} = \frac{4}{9}\frac{\left(\boldsymbol{\varepsilon}^{(\xi j)}\right)^{\mathrm{T}}\mathbf{V}}{\varepsilon_V^{(\xi j)}}\frac{\mathrm{d}\boldsymbol{\varepsilon}^{(\xi j)}}{\mathrm{d}\mathbf{D}_j}. \tag{18}$$

By substituting (18) into Eq. (13), one can obtain,

$$\frac{\mathrm{d}\mathscr{L}}{\mathrm{d}\mathbf{D}_j} = \sum_{j=1}^{J}\sum_{\xi}^{\aleph}\frac{8}{9}\left(\varepsilon_V^{(\xi j)} - \bar{\varepsilon}_V\right)\frac{\left(\boldsymbol{\varepsilon}^{(\xi j)}\right)^{\mathrm{T}}\mathbf{V}}{\varepsilon_V^{(\xi j)}}\frac{\mathrm{d}\boldsymbol{\varepsilon}^{(\xi j)}}{\mathrm{d}\mathbf{D}_j}. \tag{19}$$

Note that in the finite element formulation, $\boldsymbol{\varepsilon}^{(\xi j)}$ can be calculated as,

$$\boldsymbol{\varepsilon}^{(\xi j)} = \mathbf{B}^{(\xi j)}\mathbf{u}_j, \tag{20}$$

where $\mathbf{B}^{(\xi j)}$ denotes the strain-displacement matrix at integration point ξ, and $\mathbf{u}_j$ stands for the displacement vector of macro element j. Therefore, Eq. (19) can be rewritten as,

$$\frac{\mathrm{d}\mathscr{L}}{\mathrm{d}\mathbf{D}_j} = \sum_{j=1}^{J}\sum_{\xi}^{\aleph}\frac{8}{9}\left(\varepsilon_V^{(\xi j)} - \bar{\varepsilon}_V\right)\frac{\left(\boldsymbol{\varepsilon}^{(\xi j)}\right)^{\mathrm{T}}\mathbf{V}}{\varepsilon_V^{(\xi j)}}\mathbf{B}^{(\xi j)}\frac{\mathrm{d}\mathbf{u}_j}{\mathrm{d}\mathbf{D}_j}. \tag{21}$$

Here, one can introduce a unit index vector $\mathbf{L}_j$ for macro element j that relates its elemental displacement vector $\mathbf{u}_j$ to global displacement vector $\mathbf{U}$, expressed as,

$$\mathbf{u}_j = \mathbf{L}_j\mathbf{U}. \tag{22}$$

Thereby, Eq. (21) is changed as,

$$\frac{\mathrm{d}\mathscr{L}}{\mathrm{d}\mathbf{D}_j} = \sum_{j=1}^{J}\sum_{\xi}^{\aleph}\frac{8}{9}\left(\varepsilon_V^{(\xi j)} - \bar{\varepsilon}_V\right)\frac{\left(\boldsymbol{\varepsilon}^{(\xi j)}\right)^{\mathrm{T}}\mathbf{V}}{\varepsilon_V^{(\xi j)}}\mathbf{B}^{(\xi j)}\mathbf{L}_j\frac{\mathrm{d}\mathbf{U}}{\mathrm{d}\mathbf{D}_j}. \tag{23}$$

By calculating the derivative of global equilibrium equation $\mathbf{KU} = \mathbf{F}$ with respect to $\mathbf{D}_j$, one can have,

$$\frac{\mathrm{d}\mathbf{K}}{\mathrm{d}\mathbf{D}_j}\mathbf{U} + \mathbf{K}\frac{\mathrm{d}\mathbf{U}}{\mathrm{d}\mathbf{D}_j} = \boldsymbol{0}. \tag{24}$$

Thus, Eq. (23) can be further formulated as,

$$\frac{\mathrm{d}\mathscr{L}}{\mathrm{d}\mathbf{D}_j} = -\left[\sum_{j=1}^{J}\sum_{\xi=1}^{\aleph}\frac{8\left(\varepsilon_V^{(\xi j)} - \bar{\varepsilon}_V\right)}{9\varepsilon_V^{(\xi j)}}\left(\boldsymbol{\varepsilon}^{(\xi j)}\right)^{\mathrm{T}}\mathbf{V}\mathbf{B}^{(\xi j)}\right]\mathbf{L}_j\mathbf{K}^{-1}\frac{\mathrm{d}\mathbf{K}}{\mathrm{d}\mathbf{D}_j}\mathbf{U}. \tag{25}$$

Note that Eq. (25) can be difficult to calculate numerically due to the inverse of global stiffness matrix $\mathbf{K}$. Therefore, an adjoint vector $\boldsymbol{\lambda}$ is introduced here, which can be calculated as,

$$\mathbf{K}\boldsymbol{\lambda} = \sum_{j=1}^{J}\sum_{\xi=1}^{\aleph}\frac{8}{9}\frac{\left(\varepsilon_V^{(\xi j)} - \bar{\varepsilon}_V\right)}{\varepsilon_V^{(\xi j)}}\left(\mathbf{B}^{(\xi j)}\mathbf{L}_j\right)^{\mathrm{T}}\mathbf{V}\boldsymbol{\varepsilon}^{(\xi j)}. \tag{26}$$

Eq. (25) is then expressed as,

$$\frac{\mathrm{d}\mathscr{L}}{\mathrm{d}\mathbf{D}_j} = -\boldsymbol{\lambda}^{\mathrm{T}}\frac{\mathrm{d}\mathbf{K}}{\mathrm{d}\mathbf{D}_j}\mathbf{U}. \tag{27}$$

The sensitivity of $\mathbf{K}$ with respect to $\mathbf{D}_j$ is dependent on elemental stiffness matrix $\mathbf{k}_j$ with respect to $\mathbf{D}_j$. Thereby, Eq. (27) can be further calculated as,

$$\frac{\mathrm{d}\mathscr{L}}{\mathrm{d}\mathbf{D}_j} = -\boldsymbol{\mu}_j^{\mathrm{T}}\frac{\mathrm{d}\mathbf{k}_j}{\mathrm{d}\mathbf{D}_j}\mathbf{u}_j = -\boldsymbol{\mu}_j^{\mathrm{T}}\sum_{\xi=1}^{\aleph}\left(\mathbf{B}^{(\xi j)}\right)^{\mathrm{T}}\frac{\mathrm{d}\mathbf{H}_j}{\mathrm{d}\mathbf{D}_j}\mathbf{B}^{(\xi j)}\mathbf{u}_j. \tag{28}$$

where $\boldsymbol{\mu}_j = \mathbf{L}_j\boldsymbol{\lambda}$ denotes the elemental adjoint vector, $\mathbf{H}_j$ is the material constitutive matrix of macro element j, which can be calculated using the asymptotic homogenisation technique at the microscopic level.

Second, we derive the sensitivity at the microscopic level. The parameterised iso-truss lattice can be projected into the micro-FE model using the geometric projection technique as detailed in Section 2.2. A micro element m in the micro-FE model is then associated with a projected density ρ_m as defined in Eq. (10). According to the asymptotic homogenisation technique, a homogenised tensor component H_{pqsz} can be calculated as [1,41],

$$H_{pqsz} = \frac{1}{Y}\sum_{m=1}^{M}\left(\boldsymbol{\nu}_m^{(pq)}\right)^{\mathrm{T}}\rho_m\mathbf{k}_m\boldsymbol{\nu}_m^{(sz)}. \tag{29}$$

where Y is the volume of the whole micro-FE model, M is the total number of micro elements in the micro-FE model of the lattice unit-cell, $\boldsymbol{\nu}_m^{(pq)}$ is the elemental displacement vector of micro element m induced by unit test strain fields [1,41]. $\mathbf{k}_m$ is the micro elemental stiffness matrix with solid base materials. p, q, s and z are the indices varying from 1 to 3 for 3D cases. If we adopt notation of $(\ )_{11}\rightarrow(\ )_1$, $(\ )_{22}\rightarrow(\ )_2$, $(\ )_{33}\rightarrow(\ )_3$, $(\ )_{23}\rightarrow(\ )_4$, $(\ )_{13}\rightarrow(\ )_5$, $(\ )_{12}\rightarrow(\ )_6$, this will allow us to concisely express H_{pqsz} in a matrix form $\mathbf{H}_j$ as,

$$\mathbf{H}_j = \begin{bmatrix} H_{11} & H_{12} & H_{13} & H_{14} & H_{15} & H_{16} \\ & H_{22} & H_{23} & H_{24} & H_{25} & H_{26} \\ & & H_{33} & H_{34} & H_{35} & H_{36} \\ & & & H_{44} & H_{45} & H_{46} \\ & symm & & & H_{55} & H_{56} \\ & & & & & H_{66} \end{bmatrix}. \tag{30}$$

The sensitivity of $\mathbf{H}_j$ with respect to $\mathbf{D}_j$ can be calculated as,

$$\frac{\mathrm{d}\mathbf{H}_j}{\mathrm{d}\mathbf{D}_j} = \sum_{m=1}^{M}\frac{\mathrm{d}\mathbf{H}_j}{\mathrm{d}\rho_m}\frac{\mathrm{d}\rho_m}{\mathrm{d}\mathbf{D}_j}. \tag{31}$$

where the sensitivity of each component (H_{pqsz}) in $\mathbf{H}_j$ with respect to ρ_m can be calculated using Eq. (29) as,

$$\frac{\mathrm{d}H_{pqsz}}{\mathrm{d}\rho_m} = \frac{1}{Y}\sum_{m=1}^{M}\left(\boldsymbol{\nu}_m^{(pq)}\right)^{\mathrm{T}}\mathbf{k}_m\boldsymbol{\nu}_m^{(sz)}. \tag{32}$$

From Eq. (31), one can notice that the sensitivity calculation relies on the derivative of ρ_m with respect to $\mathbf{D}_j$. By using Eq. (10), one can have,

$$\frac{\mathrm{d}\rho_m}{\mathrm{d}\mathbf{D}_j} = \sum_{i=1}^{19}\left(\frac{\bar{\rho}_i^{(m)}}{\rho_m}\right)^{\eta-1}\frac{\mathrm{d}\bar{\rho}_i^{(m)}}{\mathrm{d}\mathbf{D}_j}. \tag{33}$$

where $\bar{\rho}_i^{(m)}$ denotes the projected density of micro element m to bar i as defined in Eq. (9). The details of the sensitivity analysis of $\bar{\rho}_i^{(m)}$ with respect to α_i can be found in [38,39]. Here, we directly use the deduced results, expressed as,

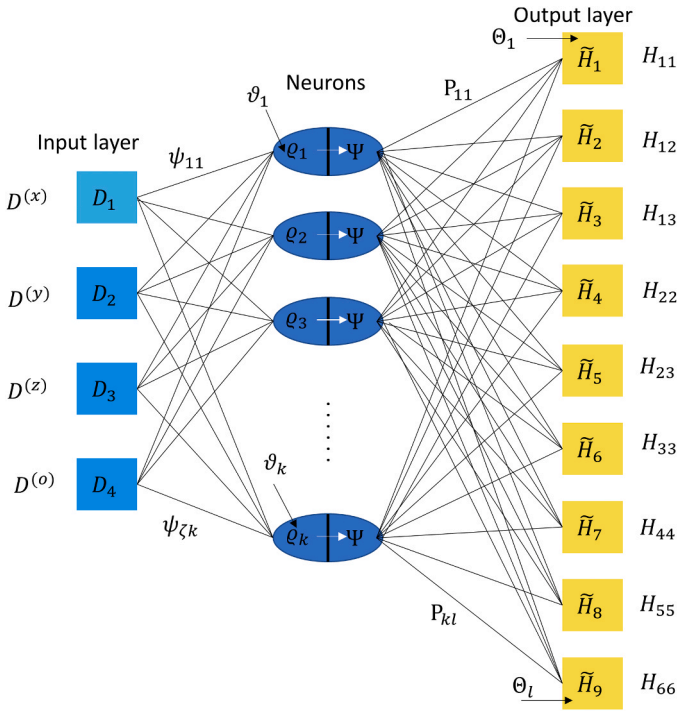

Fig. 2. The structure of the derivative-aware neural network (DANN).

$$\frac{\mathrm{d}\overline{\rho}_i^{(m)}}{\mathrm{d}\alpha_i}=\begin{cases}0, \varphi_i<-r\\ -\dfrac{3\left(\varphi_i^2-r^2\right)}{8r^3}, -r\le\varphi_i\le r\\ 0, \varphi_i>r\end{cases}, \tag{34}$$

In this study, bar i belongs to collections as,

$$i\in\mathbf{I}^x\cup\mathbf{I}^y\cup\mathbf{I}^z\cup\mathbf{I}^o, \tag{35}$$

where $\mathbf{I}^x$, $\mathbf{I}^y$, $\mathbf{I}^z$ and $\mathbf{I}^o$ denote the bar collections towards x, y, z and diagonals directions, respectively, and $\mathbf{I}^x\cap\mathbf{I}^y\cap\mathbf{I}^z\cap\mathbf{I}^o=\varnothing$. Therefore, one can calculate Eq. (33) as,

$$\frac{\mathrm{d}\rho_m}{\mathrm{d}\mathbf{D}_j}=\begin{cases}\dfrac{\mathrm{d}\rho_m}{\mathrm{d}D_j^{(x)}}=-\sum\limits_{i=1}^{19}\left(\dfrac{\overline{\rho}_i^{(m)}}{\rho_m}\right)^{\eta-1}\sum\limits_{i\in\mathbf{I}^x}\dfrac{3\left(\varphi_i^2-r^2\right)}{8r^3}\\ \dfrac{\mathrm{d}\rho_m}{\mathrm{d}D_j^{(y)}}=-\sum\limits_{i=1}^{19}\left(\dfrac{\overline{\rho}_i^{(m)}}{\rho_m}\right)^{\eta-1}\sum\limits_{i\in\mathbf{I}^y}\dfrac{3\left(\varphi_i^2-r^2\right)}{8r^3}\\ \dfrac{\mathrm{d}\rho_m}{\mathrm{d}D_j^{(z)}}=-\sum\limits_{i=1}^{19}\left(\dfrac{\overline{\rho}_i^{(m)}}{\rho_m}\right)^{\eta-1}\sum\limits_{i\in\mathbf{I}^z}\dfrac{3\left(\varphi_i^2-r^2\right)}{8r^3}\\ \dfrac{\mathrm{d}\rho_m}{\mathrm{d}D_j^{(o)}}=-\sum\limits_{i=1}^{19}\left(\dfrac{\overline{\rho}_i^{(m)}}{\rho_m}\right)^{\eta-1}\sum\limits_{i\in\mathbf{I}^o}\dfrac{3\left(\varphi_i^2-r^2\right)}{8r^3}\end{cases}, -r\le\varphi_i\le r, \tag{36}$$

Thus, by combining Eqs. (28), (31), (33), and (36), one can obtain the sensitivity of $\mathscr{L}$ with respect to $\mathbf{D}_j$ analytically.

2.4. Derivative-aware neural network (DANN)

As the design domain is infilled with non-uniform iso-truss lattices $j\in[1, J]$, micro-FE analyses and sensitivity analyses are required to be performed repeatedly on every lattice j. Apparently, the computational burden of this FE^2 method can be prohibitive, especially for the design optimisation intrinsically associated with multi-iterations.

In order to tackle this issue, we adopt a derivative-aware neural network (DANN) to output the homogenised elastic tensor H_{pqsz} and its sensitivity with respect to design variables $\mathbf{D}_j$. Fig. 2 illustrates the structure of the DANN, which comprises an input layer, a hidden layer (neurons) and an output layer. The input layer is composed of 4 inputs (D_1, D_2, D_3 and D_4) representing design variables corresponding to $D^{(x)}$, $D^{(y)}$, $D^{(z)}$, $D^{(o)}$, respectively. As the parameterised iso-truss lattice has orthotropic properties, the DANN output 9 independent elastic tensor components as demonstrated in Fig. 2, where $\widetilde{H}_1, \widetilde{H}_2, \widetilde{H}_3, \widetilde{H}_4, \widetilde{H}_5, \widetilde{H}_6, \widetilde{H}_7, \widetilde{H}_8, \widetilde{H}_9$ are the elastic tensors obtained from the DANN corresponding to $H_{11}, H_{12}, H_{13}, H_{22}, H_{23}, H_{33}, H_{44}, H_{55}$ and H_{66} in $\mathbf{H}_j$. The hidden layer with neurons is used to calculate the response from the input layer and approximate the response to the output layer.

In Fig. 2, $\psi_{\zeta k}$ is the weight factor of input variable ζ to neuron k for calculating response ϱ_k, ϑ_k is a bias parameter associated with neuron k. For instance, ψ_{11} denotes the weight factor of input variable D_1 to neuron 1. And ϑ_1 is the bias parameter associated with neuron 1. Ψ represents an activation function with the input value of ϱ_k.

In order to obtain accurate outputs, one needs to train the neural networks using a ground-truth dataset. In other words, the training process enables to find the optimal weight factors $\psi_{\zeta k}$, P_{kl} and bias pa-

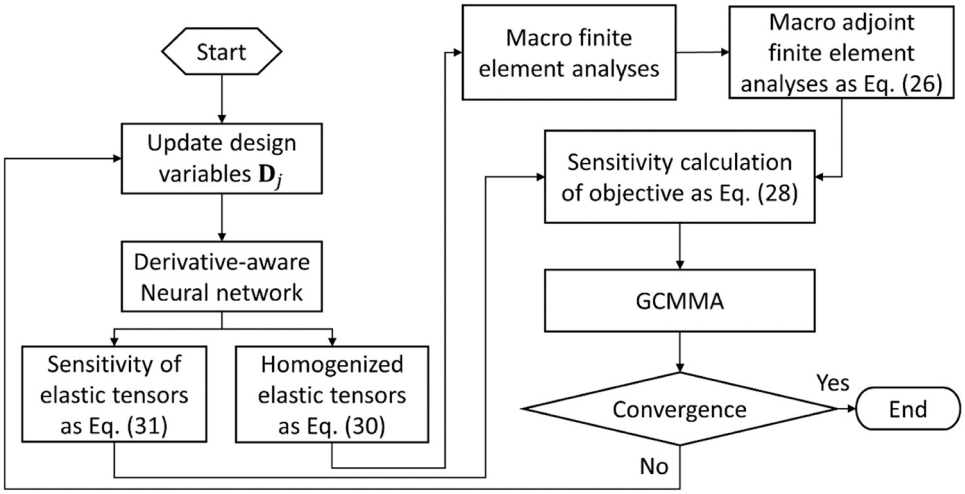

Fig. 3. A flowchart of the proposed multiscale optimisation based on a derivative-aware neural network (DANN).

Table 1
Algorithm of the DANN-based multiscale optimisation framework for design of non-uniform lattice structures.

i) Set initial design variables $\mathbf{D}_j$ $\left(D_j^{(x)}, D_j^{(y)}, D_j^{(z)}, D_j^{(o)}\right)$ for each lattice j.

ii) Homogenisation:

for each lattice j, **do**

input: $D_j^{(x)}, D_j^{(y)}, D_j^{(z)}, D_j^{(o)} \rightarrow$ DANN $\rightarrow \widetilde{H}_1, \widetilde{H}_2, \widetilde{H}_3, \widetilde{H}_4, \widetilde{H}_5, \widetilde{H}_6, \widetilde{H}_7, \widetilde{H}_8, \widetilde{H}_9 \rightarrow \frac{\partial \widetilde{H}_l}{\partial \mathbf{D}_j}$

end for

iii) Macro-FE analysis:

$\mathbf{KU} = \mathbf{F}$ as defined in Eq. (12).

iv) Adjoint macro-FE analysis

$\mathbf{K\lambda} = \sum_{j=1}^{J} \sum_{\xi=1}^{\aleph} \frac{8}{9} \frac{\left(\varepsilon_V^{(\xi,j)} - \overline{\varepsilon}_V\right)}{\varepsilon_V^{(\xi,j)}} \left(\mathbf{B}^{(\xi,j)} \mathbf{L}_j\right)^{\mathrm{T}} \mathbf{V} \boldsymbol{\varepsilon}^{(\xi,j)}$ as defined in Eq. (26).

v) Calculate the sensitivity of the objective with respect to design variables $\mathbf{D}_j$:

for each lattice j, **do**

$\frac{\mathrm{d}\mathcal{L}}{\mathrm{d}\mathbf{D}_j} = -\boldsymbol{\mu}_j^{\mathrm{T}} \frac{\mathrm{d}\mathbf{k}_j}{\mathrm{d}\mathbf{D}_j} \mathbf{u}_j = -\boldsymbol{\mu}_j^{\mathrm{T}} \sum_{\xi=1}^{\aleph} \left(\mathbf{B}^{(\xi,j)}\right)^{\mathrm{T}} \frac{\mathrm{d}\mathbf{H}_j}{\mathrm{d}\mathbf{D}_j} \mathbf{B}^{(\xi,j)} \mathbf{u}_j$ as defined in Eq. (28).

$\frac{\mathrm{d}\mathbf{H}_j}{\mathrm{d}\mathbf{D}_j}$ is approximated by $\frac{\partial \widetilde{H}_l}{\partial \mathbf{D}_j}$ calculated in (ii).

end for

vi) Input the objective $\mathcal{L}$ and the sensitivity $\frac{\partial \widetilde{H}_l}{\partial \mathbf{D}_j}$ to the optimisation solver GCMMA.

vii) **If** converge, **then**

exit.

else

Update design variables $\mathbf{D}_j$ $\left(D_j^{(x)}, D_j^{(y)}, D_j^{(z)}, D_j^{(o)}\right)$

go to (ii), (iii), (iv), (v), (vi).

end if

rameters ϑ_k, Θ_l to satisfy the following loss function for a conventional neural network (NN) as,

$$\underset{\psi_{\zeta k}, P_{kl}, \vartheta_k, \Theta_l}{\operatorname{argmin}} \sum_{l=1}^{9} \left[\widetilde{H}_l(D_\zeta, \psi_{\zeta k}, P_{kl}, \vartheta_k, \Theta_l) - H_l\right]^2, \tag{37}$$

where $l \in [1, 9]$ is the number of outputs,P_{kl} denotes the weight factor of neuron k to output $\widetilde{H}_l$. Θ_l denotes the bias parameter associated with output $\widetilde{H}_l$, H_l stands for the components of actual elastic tensors calculated by the FE-based homogenisation as defined by Eq. (29).

Although Eq. (37) can ensure accurate outputs, derivative $\frac{\partial \widetilde{H}_l}{\partial D_\zeta}$ may not align with the actual derivative $\frac{\partial H_l}{\partial D_\zeta}$. Note that the derivative, namely the sensitivity defined in Eq. (31), is necessary for solving the optimisation problem. For this purpose, we propose the DANN trained by both actual response H_l and the actual sensitivity $\frac{\partial H_l}{\partial D_\zeta}$. In other words, the DANN's training process incorporates the actual sensitivity information. This means that the DANN is guided by the underlying sensitivity information obtained from the FE-based homogenisation analysis, making it truly derivative-aware. Thus, a modified loss function by adding the error of derivatives between the DANN and FE-derived is expressed as,

$$\underset{\psi_{\zeta k}, P_{kl}, \vartheta_k, \Theta_l}{\operatorname{argmin}} \sum_{l=1}^{9} \left[\left(\widetilde{H}_l(D_\zeta, \psi_{\zeta k}, P_{kl}, \vartheta_k, \Theta_l) - H_l\right)^2 + \sum_{\zeta=1}^{4} \left(\frac{\partial \widetilde{H}_l}{\partial D_\zeta} - \frac{\partial H_l}{\partial D_\zeta}\right)^2\right]. \tag{38}$$

Consequently, the derivative of the trained DANN satisfying Eq. (38) can

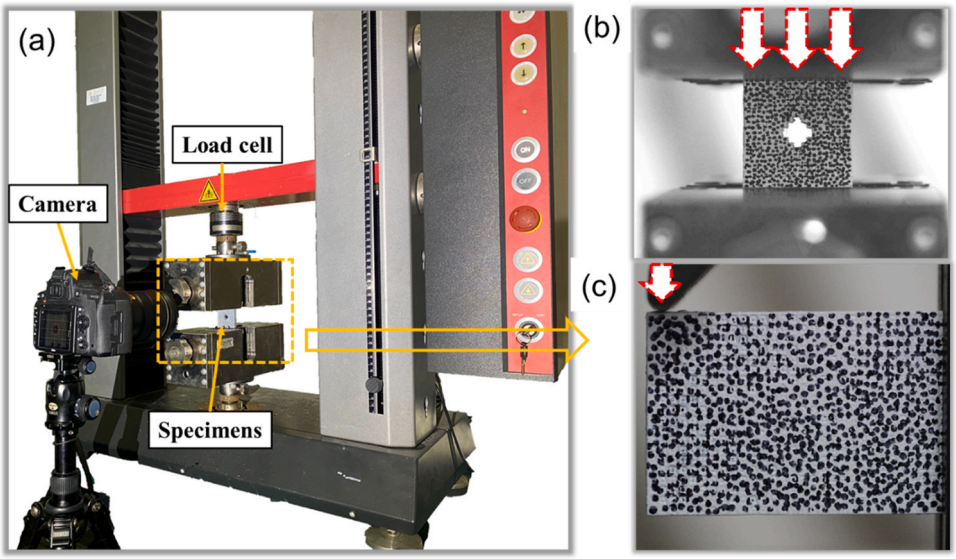

Fig. 4. The experimental setups for the cantilever and compressive tests respectively. (a) The set-up of the experimental tests. (b) The quasi-static compressive tests. (c) The cantilever bending tests.

directly approximate the sensitivity, which can be employed to provide gradient information in iteration processes.

In this study, three different activation functions Ψ_1, Ψ_2 and Ψ_3 are investigated. The first activation function, Ψ_1, is a so-called sigmoid or logistic activation function, expressed as,

$$\Psi_1(\varrho_k) = \frac{1}{1+e^{-\varrho_k}}, \tag{39}$$

And its derivate is calculated as,

$$\Psi_1^{'}(\varrho_k) = \Psi_1(\varrho_k)[1-\Psi_1(\varrho_k)]. \tag{40}$$

The second activation function, Ψ_2, is based on a hyperbolic tangent activation function, expressed as,

$$\Psi_2(\varrho_k) = \frac{2}{1+e^{-2\varrho_k}} - 1, \tag{41}$$

and its derivative is calculated as,

$$\Psi_2^{'}(\varrho_k) = 1-[\Psi_2(\varrho_k)]^2, \tag{42}$$

The third, Ψ_3, is chosen to be a Gaussian function, expressed as,

$$\Psi_3(\varrho_k) = e^{-\varrho_k{}^2}. \tag{43}$$

And its derivative is calculated as,

$$\Psi_3^{'}(\varrho_k) = -2\varrho_k\Psi_3(\varrho_k), \tag{44}$$

As the number of neurons can affect the performance of the trained DANN, five different hidden layers with the number of neurons 30, 50, 100, 150, and 200 were also tested in our study. The training of the DANN was based on a backpropagation scheme [42], in which the sensitivity $\frac{\partial \tilde{H}_l}{\partial D_\zeta}$ with respect to $\psi_{\zeta k}, P_{kl}, \vartheta_k, \Theta_l$ were used as the gradient information for a limited-memory Broyden–Fletcher–Goldfarb–Shanno (L-BFGS) optimisation algorithm [43] to solve Eq. (38).

In this study, we used 2000 sampling points generated by the Latin hypercube sampling method [44] ranging from 0.3 to 0.7 and computed from the micro-FE analyses as the ground-truth data for the training process. 400 additional sampling points ranging from 0.3 to 0.7 randomly generated and calculated from micro-FE analyses were employed as a test dataset. The training epoch defining the times that L-BFGS works through the entire training data was set as 10,000. To prevent the L-BFGS from being stuck in a local minimum, a different weight initialisation technique [45] was employed, in which the weight factors $\psi_{\zeta k}$, P_{kl} and bias parameters ϑ_k, Θ_l were randomly generated ranging from − 0.01–0.2.

After the training process, the DANN is integrated with macro-FE analyses for optimisation. Fig. 3 illustrates the flowchart of the proposed optimisation procedure on the basis of the DANN. A globally convergent version of the method of moving asymptotes (GCMMA) [46] was employed to update design variables $\mathbf{D}_j$. A detailed pseudo-code is also provided in Table 1 to clarify the proposed framework.

2.5. 3D fabrication by powder bed fusion (PBF)

Ti6Al4V was used as the feedstock powder which has a Young's modulus of 105 GPa and a Poisson's ratio of 0.3. The optimised designs were fabricated by powder bed fusion (PBF) using a commercial EOS M300 system (EOS GmbH, Germany). Process parameters for the fabrication were set as follows: layer thickness 30 μm, scanning speed 1200 mm/s, laser power 280 W, and hatch distance 0.14 μm. After fabrication, all the samples were carefully cleaned with compressed air to remove residual powders. After removing the samples from the building plate, a proper heat treatment process was followed with a heating rate of 10 ℃/min in a nitrogen environment. The temperature was maintained at 800 ℃ for 2 h. The samples were removed from the furnace and cooled naturally at a rate of 6 ℃/min to the environment temperature.

2.6. Mechanical tests with digital image correlation (DIC)

The compressive and cantilever tests were conducted in the universal testing machine Zwick Z010 (Zwick GmbH of Germany), with a load cell capacity of 10 kN in the ambient temperature and humidity (25 °C, 33% RH). To observe the strain distribution in the sample, digital image correlation (DIC) technique was employed here. Before the speckle patterns were sprayed on the front surface of the specimen, soft paint was placed to fill the pores of cells on the front surface. The setup of the experiments is shown in Fig. 4.

For the quasi-static compressive tests, the bottom and top of the plate (fully dense structure) were respectively clamped and loaded to 3000 N with a speed of 0.1 mm/min (Fig. 4(b)). For the cantilever bending tests,

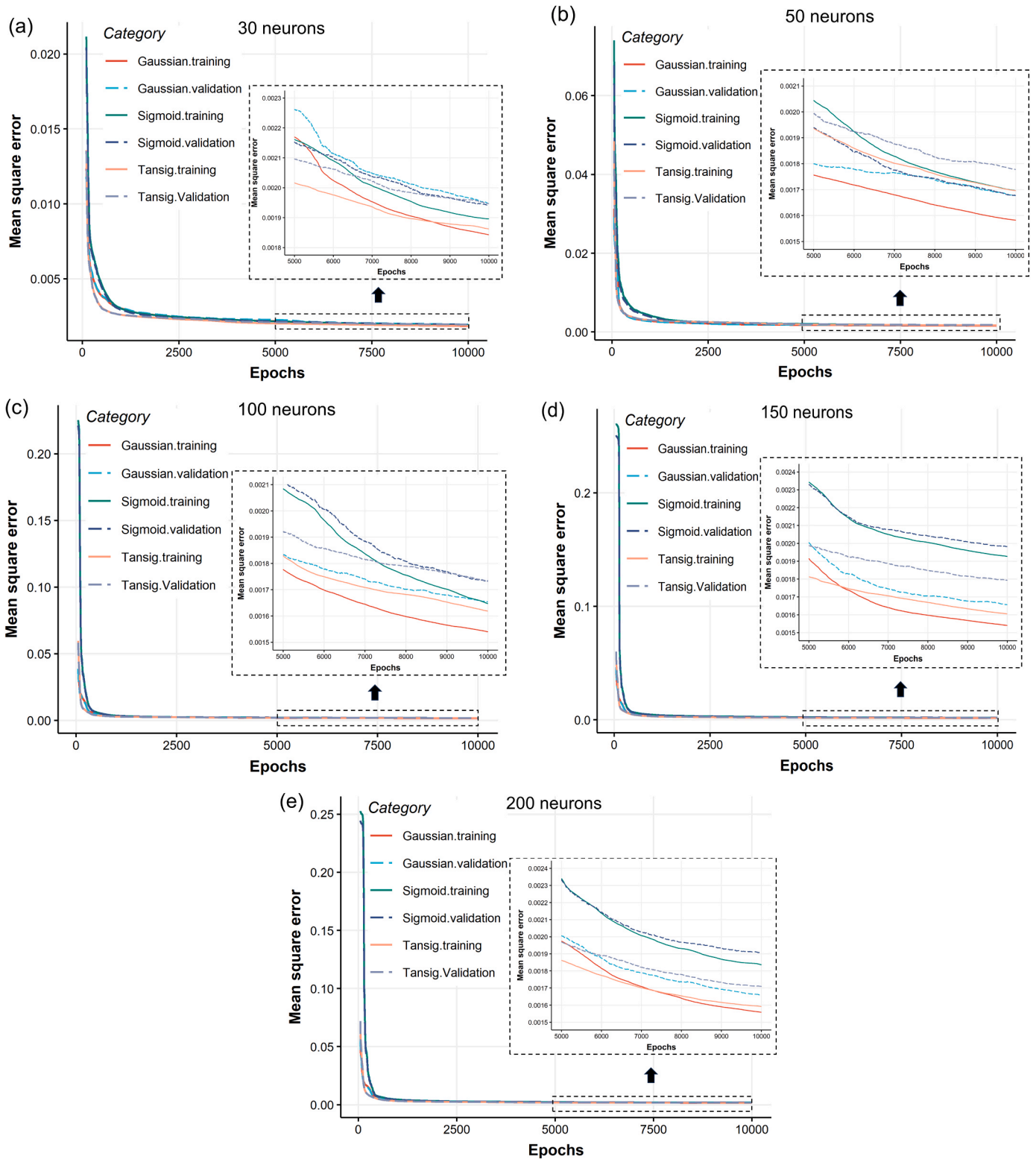

Fig. 5. Learning curves of different derivative-aware neural network (DANN) models calculated on the training dataset and testing dataset. (a) – (e) DANNs with the 30, 50, 100, 150, 200 neurons.

the right-hand side of the specimen (fully dense structure) was fully fixed, and the top surface of the left-hand side was loaded to 750 N by a 5 mm diameter round head with a speed of 0.1 mm/min (Fig. 4(c)).

A 6000 × 4000 pixels CCD camera with a lens of 150 mm focal length was used to acquire one image per second. The postprocessing of the digital images was performed in the DIC professional software VIC-2D (CSI, USA) [47]. To ensure computational accuracy, the facet size and facet step were respectively set to be 61 × 61 pixels and 15 × 15 pixels to calculate the displacement and strain fields of the front face of these samples.

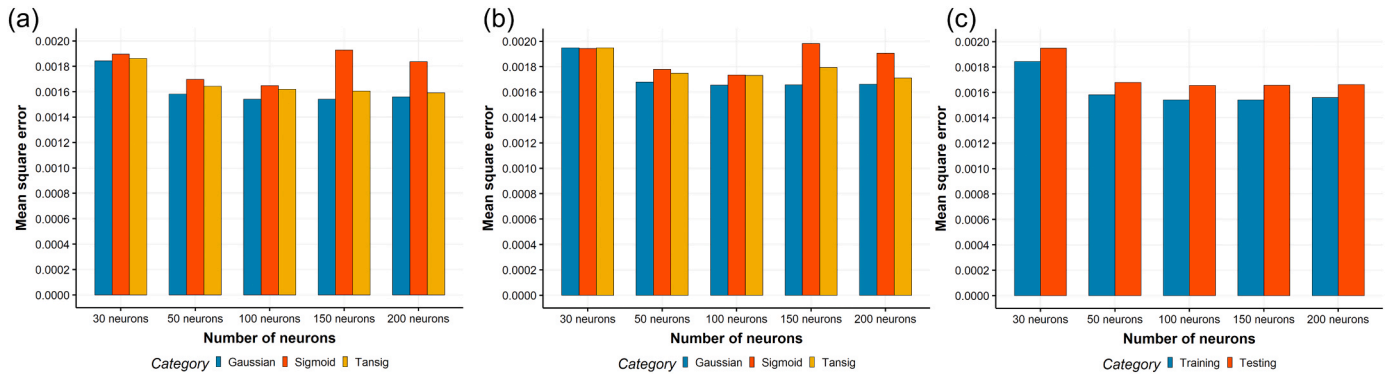

Fig. 6. Comparison of mean square errors (MSEs) for the different derivative-aware neural networks (DANNs). (a) MSEs on training dataset; (b) MSEs on the testing dataset. DANNs with 30, 50, 100, 150, and 200 neurons in the hidden layer are compared; DANNs with the three different activation functions, including Gaussian, Sigmoid, and tansig, are compared. (c) MSEs on the training and testing datasets are compared for the DANN using 30, 50, 100, 150, and 200 neurons in the hidden layer and the Gaussian activation function.

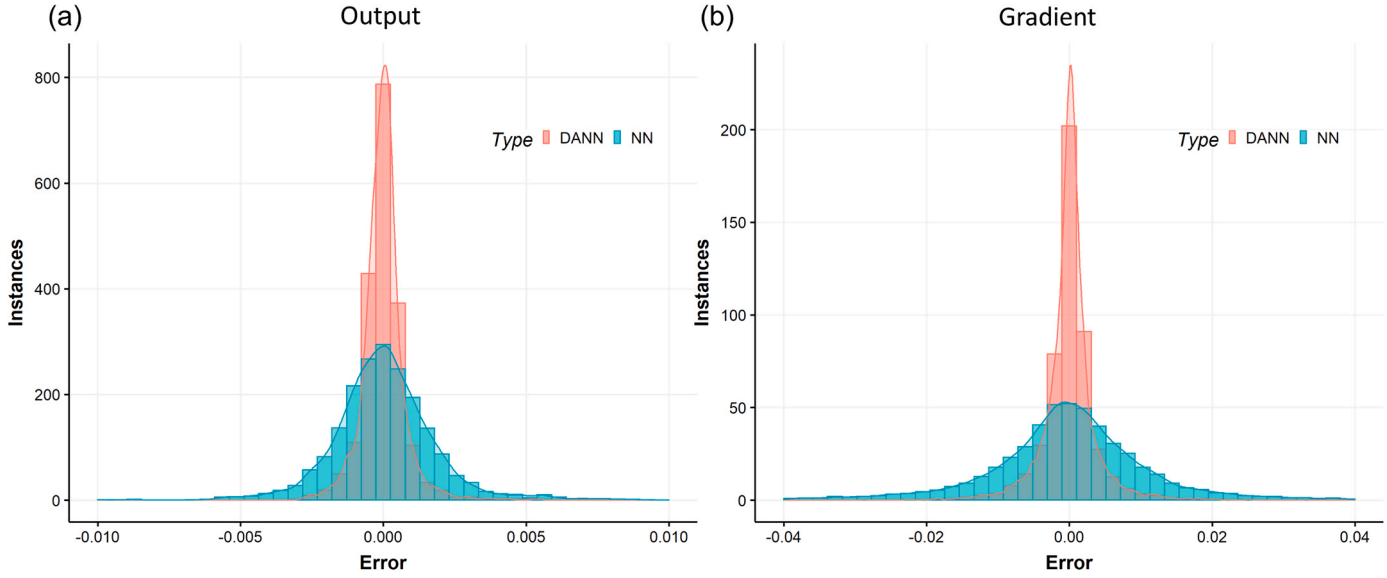

Fig. 7. Histogram of the errors based on the derivative-aware neural network (DANN) and the conventional neural network (NN). The conventional NN and the DANN have the same structure but are trained with the loss function without and with the sensitivity information, respectively. (a) Comparison of the histograms of the output errors based on the DANN and NN, respectively; (b) Comparison of the histograms of the gradient errors based on the DANN and the NN. Both errors are calculated from the testing dataset. The DANN and NN are composed of one hidden layer through the 100 neurons with the Gaussian activation function.

3. Results

3.1. DANN performances in general

The trained DANNs with different numbers of neurons and activation functions were compared herein to investigate their performances for predicting the homogenised elastic tensors and the corresponding gradient information. To visualise the training process, Fig. 5 plots the learning curves of the 15 different DANNs calculated on the training dataset and testing dataset, which demonstrates that the training processes converged very well and all DANNs were not overfitted [12]. In addition, Fig. 6(a) evaluates the mean square errors (MSEs) of the 15 different DANNs based on the training dataset, which exhibits fairly good performances of the trained DANNs with a single hidden layer. For sake of trade-off on training time, multi-hidden layers were not tested here as it would dramatically increase the computational cost for calculation of the first derivate and second derivate in training processes [12].

In Fig. 6(a), the 15 DANNs were divided into five main groups according to the number of neurons (i.e. 30, 50, 100, 150, and 200). The DANNs using the different activation functions Ψ_1, Ψ_2 and Ψ_3, as defined in Section 2.6, were compared in each group. It was found that all five groups achieved fairly low MSEs, all less than 0.002. The DANN using the Gaussian activation function in each group has the minimum MSE, whereas that using the Sigmoid activation function has a higher MSE than those using the hyperbolic tangent activation function.

The MSEs slightly decreased when the number of neurons increased from 30 to 100 and then marginally went up with the further increase of neurons from 100 to 200. The DANN using 100 neurons and the Gaussian activation function achieved the minimum MSE (0.00154) of all the 15 DANNs here. A similar trend can be also found in terms of the MSEs calculated on the testing dataset (Fig. 6(b)), where the DANN using 100 neurons and the Gaussian activation function dominates the others with a minimum MSE (0.00165). Fig. 6(c) compares the MSEs on the training and testing datasets for the DANNs with the Gaussian activation function, in which all the MSEs calculated on the testing dataset are slightly higher than those on the training dataset. Nevertheless, the DANNs demonstrate excellent predictive capability with the fairly low MSEs calculated on the testing dataset. After comparing DANNs with the different neurons and activation functions, the DANN

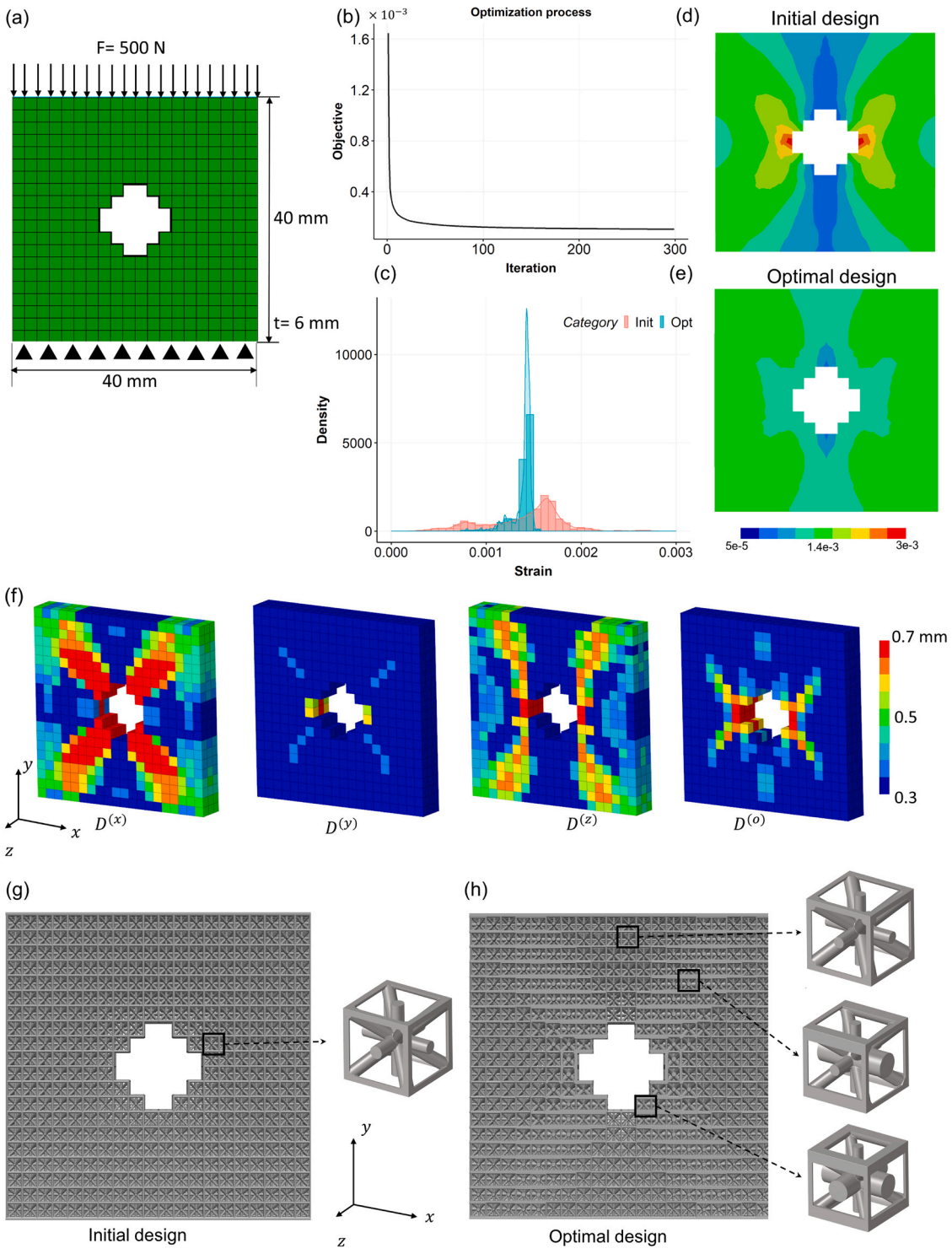

Fig. 8. Comparison of the optimised and the initial designs of the squared plate with a centre hole. (a) The macro FE model and boundary conditions; (b) The iteration history of the design objective; (c) Histograms of equivalent strains obtained from the initial and optimal designs respectively. (d) The contour of the equivalent strain in the design domain of the initial design. (e) The contour of the equivalent strain in the design domain of the optimal design. (f) The contour of design variables $D^{(x)}$,$D^{(y)}$,$D^{(z)}$,$D^{(o)}$; (g) The full lattice model of the initial design and its micro-unit-cell. (h) The full lattice models of the optimal design and its micro unit-cells at different locations.

with 100 neurons and the Gaussian activation was thus chosen as the model for the design optimisation in this study.

Fig. 7(a) compares the histogram of errors for the output of homogenised elastic tensor calculated on the testing dataset to explore the advantages of the DANN over the conventional NN. The conventional NN and DANN both employed the same number of neurons (100 neurons) in the hidden layer with four design variables in the input layer to predict the homogenised elastic tensor and sensitivity. However, the training of the conventional NN was distinctly based on the loss function as defined in Eq. (37). Note that while the majority of the errors of the DANN and the conventional NN are less than 0.01, with mean values near 0, the DANN evidently exhibits a more minor standard deviation

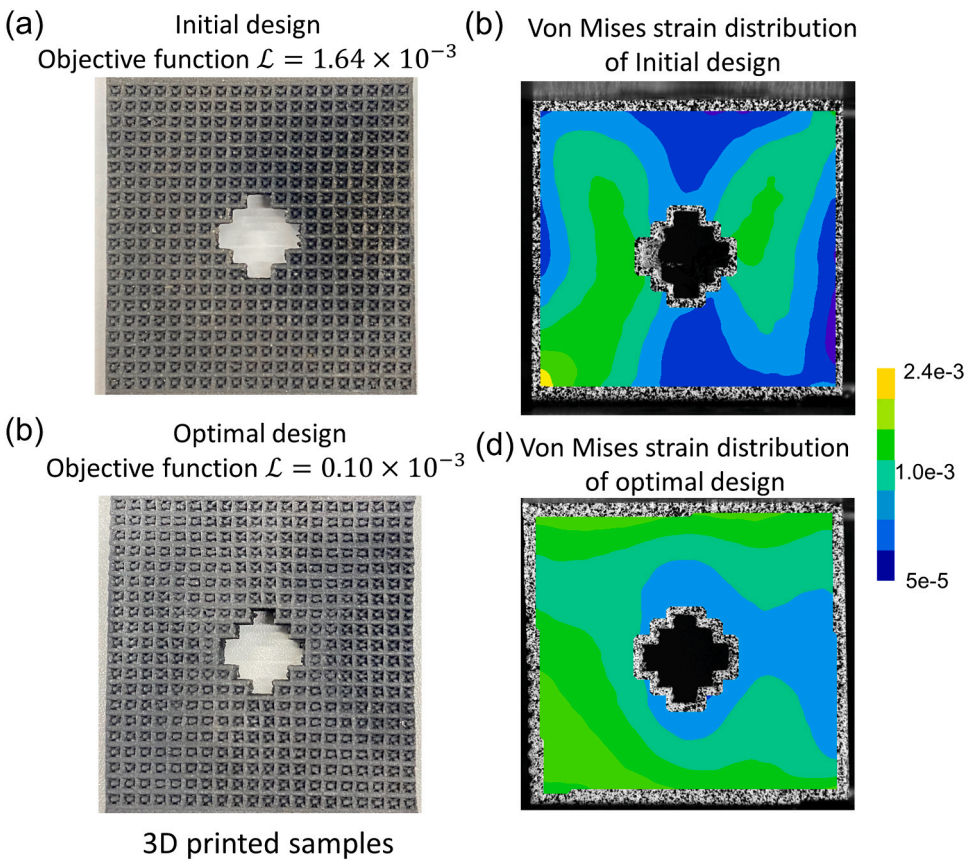

Fig. 9. The 3D printed lattices and experimental tests. (a) The 3D-printed lattice structure based on the initial design with the objective function $\mathscr{L} = 1.64 \times 10^{-3}$. (b) The equivalent strain contour on the 3D printed initial design from the DIC measurement. (c) The 3D-printed lattice structure based on the optimal design with the objective function $\mathscr{L} = 0.10 \times 10^{-3}$. (d) The equivalent strain contour on the 3D printed optimal design from the DIC measurement.

than the conventional NN.

Fig. 7(b) plots the histogram of gradient errors from the DANN and the conventional NN. It is found that the standard deviation of the DANN is much less than that of the conventional NN, demonstrating the advantage of the DANN for predicting the gradient information.

3.2. Centre hole plate

The first example is a squared plate with a hole in its central region, as shown in Fig. 8(a). The dimension of the plate is 40 × 40 mm with a thickness of 6 mm. The macro model of the plate was meshed by brick elements with an edge size of 2 mm. The bottom surface of the macro model was fully fixed and an evenly distributed in-plane load was applied on the top surface of the macro model with a total magnitude of 500 N.

In the design domain (Fig. 8(a)), each macro element j represents an iso-truss lattice unit-cell associated with the four design variables $D_j^{(x)}$, $D_j^{(y)}, D_j^{(z)}, D_j^{(o)}$ at the microscopic level. The targeted strain $\overline{\varepsilon}_V$ was set to be 0.0014, which was obtained from the initial design filled by uniform iso-truss lattices with a struct size of 0.35 mm. The lower and upper bounds ($\mathbf{D}^{\mathrm{L}}$ and $\mathbf{D}^{\mathrm{U}}$) of the design variable vector were respectively set to be 0.3 mm and 0.7 mm for the consideration of PBF printing.

Fig. 8(b) illustrates the iteration history of the objective function as defined in Eq. (12) during the optimisation process. The objective function started from 1.64×10^{-3} and was significantly decreased to 1.04×10^{-4}. Fig. 8(c) compares the density distribution of the equivalent strains calculated at the Gaussian integration points from the initial and optimised designs. The histogram of equivalent strain from the optimal design has a mean value close to the targeted strain $\overline{\varepsilon}_V$ (1.4×10^{-3}) and substantially lower standard deviation than that of the initial design. Fig. 8(d) and (e) display the equivalent strain contours in the initial and optimised designs, respectively. Evidently, the optimal design achieved a more uniform equivalent strain distribution, demonstrating the effectiveness of the proposed framework.

Fig. 8(f) illustrates the distribution of the optimised $D^{(x)}$, $D^{(y)}$, $D^{(z)}$, and $D^{(o)}$ in the design domain. It can be observed that the bars toward x and z directions play more significant role than those in y and diagonal directions in achieving the as-possible uniform strain pattern. Moreover, the lattices around the hole were much reinforced in order to reduce the high strain concentration presented in the initial design, as shown in Fig. 8(d). Fig. 8(g) and (h) illustrate the full lattice models based on the initial and optimised designs as well as the representative unit-cells at different locations, respectively, which were prepared in a STL format and ready for PBF printing. It is noted that the full lattice models comprise an upper and lower solid edge to be the clamped areas for the quasi-static compressive tests.

The DIC tests were conducted on the lattice specimens fabricated by PBF to validate the optimal results. Fig. 9(a) and (c) show the fabricated lattice specimens based on the initial design and optimal design, respectively. Fig. 9(b) and (d) present the equivalent strain distributions within the 3D printed initial design and optimal design, respectively. The equivalent strain contour was measured by the DIC system with the same load ($F = 500\ N$) as used in the design optimisation. From the DIC results, apparently, the optimised design exhibits a more uniform distribution of equivalent strain compared to the initial counterpart, further demonstrating that the proposed design framework can improve the uniformity of strain distribution in an effective fashion.

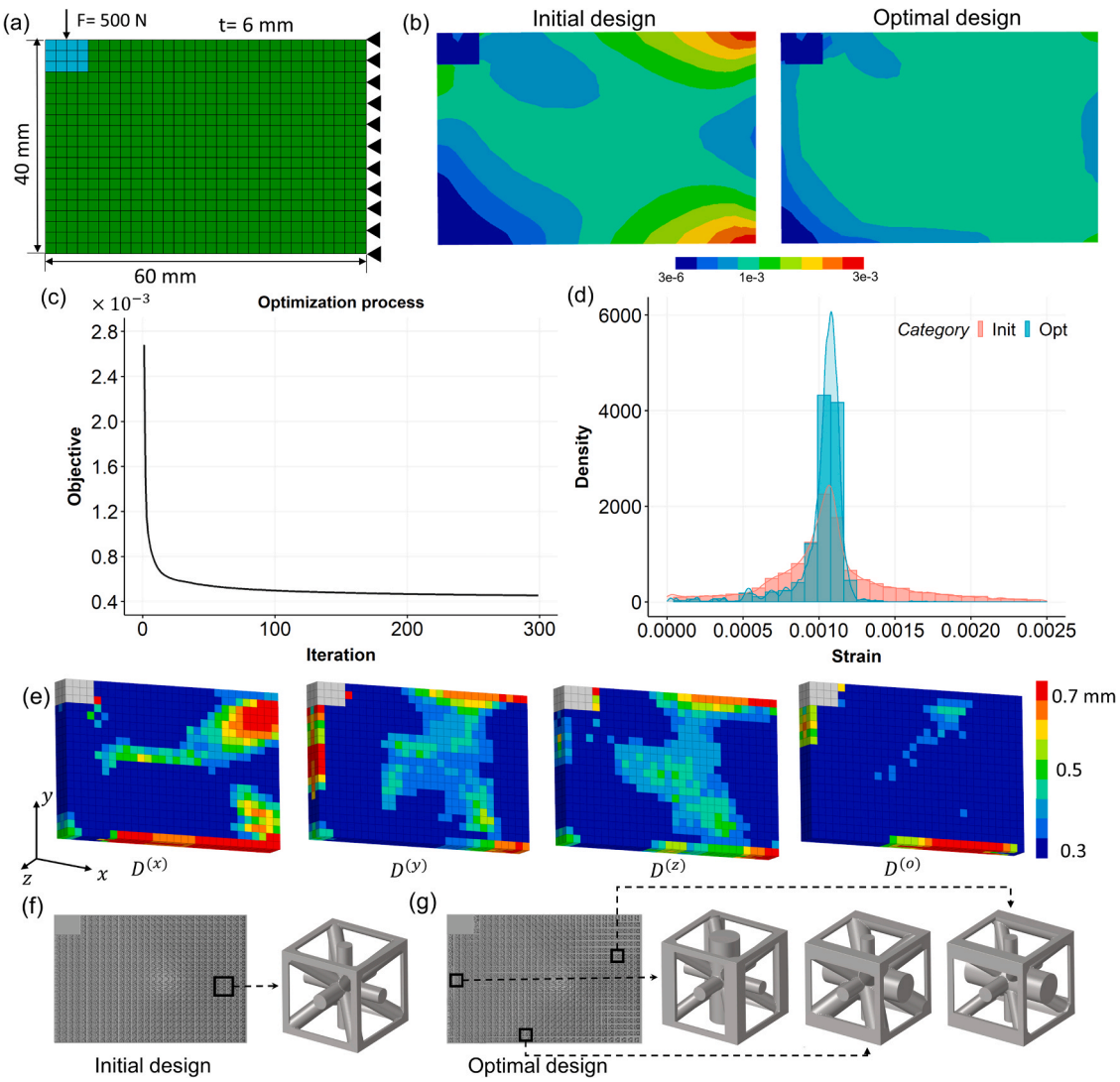

Fig. 10. The optimal and initial design results of the cantilever structure. (a) The macro finite element model and its boundary condition; (b) The equivalent strain distribution within the initial and optimal designs; (c) The iteration history of the objective function; (d) Comparison of the histogram of equivalent strain density in the initial and optimal designs. (e) The distributions of the optimised design variables in the design domain. (f) The full lattice model of the initial design with the uniform iso-truss lattices. (g) The full lattice model of the optimal design with the representative non-uniform iso-truss lattices in different regions.

3.3. Cantilever beam

The second example is a cantilever beam structure, as shown in Fig. 10(a). The dimension of the cantilever structure is 60 × 40 mm with a thickness of 6 mm. The cantilever beam was meshed by cubic elements with a size of 2 mm. The right-hand side surface was fully fixed. An evenly distributed in-plane line force of 500 N was applied at the top-left edge of 4 mm from the corner. The initial design variables and their lower and upper bounds were set to be the same as those in Section 3.2. The target strain $\overline{\varepsilon}_V$ was set to be 0.00108 obtained from the average of equivalent strain in the initial design.

Fig. 10(c) shows the iteration history of the design objective during the optimisation process, which started from 2.8×10^{-3} in the initial design and then notably dropped to 4.5×10^{-4} in the optimal design after around 300 iterations. Fig. 10(d) compares the histogram of equivalent strain obtained from the initial and optimised designs. It is noted that the initial design has a substantially higher standard deviation than the optimal design, exhibiting the effectiveness of the proposed optimisation framework. The achieved uniform strain pattern can also be observed by comparing the strain contours, as shown in Fig. 10(b).

Fig. 10(e) illustrates the distributions of the optimised design variables in the cantilever structure. It can be noted that $D^{(x)}$ plays a significant role in achieving the uniform strain pattern, where the right upper and bottom corners were reinforced to reduce the equivalent strain. The bottom surface was also strengthened to mitigate the deflection.

Fig. 10(f) and (g) show the full lattice models prepared in a STL format based on the initial and optimised designs with the details of their micro unit-cells. Fig. 11(a) and (c) exhibit the fabricated specimens based on the initial design and optimal design using the PBF technique, respectively. Fig. 11 (b) and (d) illustrate the distributions of equivalent strains in the initial and optimised designs obtained from the DIC measurements. It can be observed that the optimal design shows a more uniform strain pattern than that of the initial counterpart.

3.4. Mandibular reconstruction

The third example is a mandibular reconstruction case, as shown in Fig. 12(a). The mandibular model was constructed based on the CT data from a specific patient [48]. The mandibular bone at the left side region was sectioned to simulate a serve bone defect treated by a bone scaffold (Fig. 12(a)). The mandibular scaffold was positioned by a fixation plate

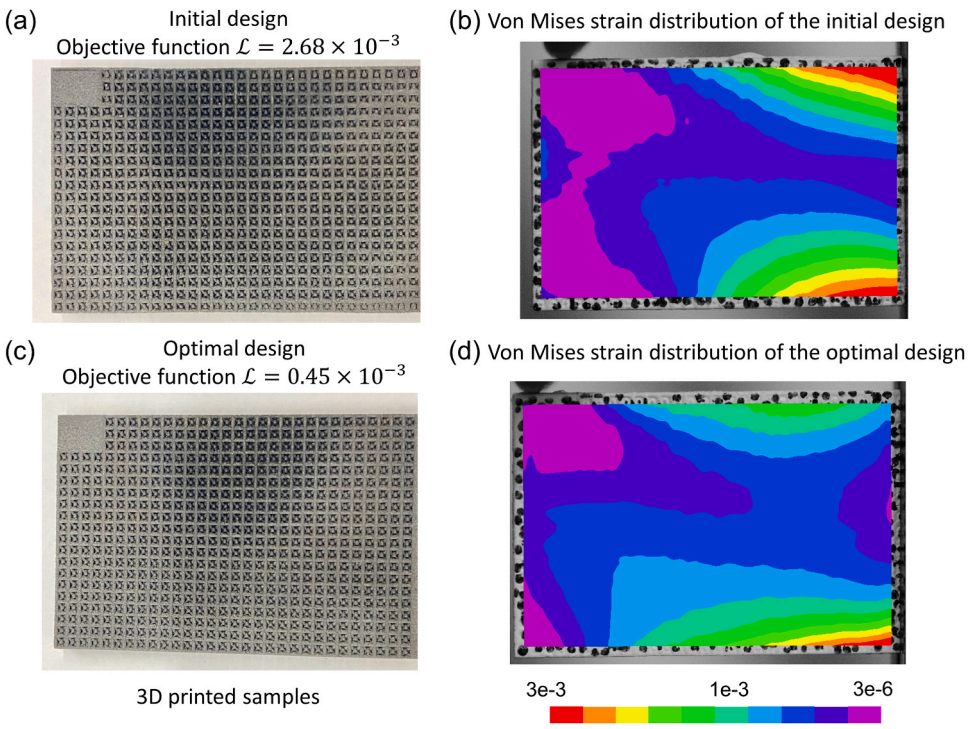

Fig. 11. The printed cantilever structures and the results of DIC tests. (a) The 3D-printed samples based on the initial design with the objective function value $\mathscr{L} = 2.68 \times 10^{-3}$. (b) The equivalent strain distributions in the initial design obtained from DIC measurement. (c) The 3D-printed samples based on the initial design with the objective function value $\mathscr{L} = 0.45 \times 10^{-3}$. (d) The equivalent strain distributions in the optimal design obtained from the DIC test.

and discretised into 400 brick elements (2 mm in size) for the design optimisation. The bony tissue was featured with CT-based heterogeneous distribution by interpolating the lowest and highest densities in terms of the Hounsfield units [49]. The loading and boundary conditions are illustrated in Fig. 12(a). The upper regions of the condyle were fully fixed, and two bitting forces ($F_1 = 60\ N$ and $F_2 = 110\ N$) measured from a clinical experiments were applied at the front tooth region [48]. The target equivalent strain $\bar{\varepsilon}_V$ was set to be 0.001, which was recommended by several clinical studies for promoting bone growth [50–53]. The initial design of the scaffold is composed of uniform iso-truss lattices with a bar size of 0.35 mm.

Fig. 12(b) shows the iteration history in the course of the optimization, in which the objective function dropped from 0.741 to 0.445 over 300 iterations. The effectiveness of the optimised design can also be noted by comparing the histograms of equivalent strain from the initial and optimised designs, as shown in Fig. 12(c). Apparently, the optimal design achieved the equivalent strain distribution with a mean value of 0.001 and less standard deviation than the initial design. Fig. 12(e) also compares the strain contours obtained from the initial and optimised designs, further exhibiting the effectiveness of the proposed method for achieving a as-possible uniform strain pattern. Fig. 12(d) illustrates the distributions of the optimised design variables and the details of non-uniform unit-cells. It can be seen that the surface areas of the scaffold were reinforced in terms of a large struct size in x, y, and z directions.

3.5. Femur bone reconstruction

The fourth example is a femur bone reconstruction case, as shown in Fig. 13(a). A 3-cm-long segmental defect was modelled in the femur bone, which is treated by a bone scaffold and stabilised using a fixation plate. The distal end of the femur was fully constrained, and a force was applied on the femur head to simulate gait loading equivalent to 1.6 times human body weight [13]. The scaffold has a hollow channel miming the medullary cavity and was discretised by 8-node cubic elements with 2800 elements.

In this design example, the objective function dropped from 7.4×10^{-3} to 2.2×10^{-3} during the optimisation process, as illustrated in Fig. 13(b). Fig. 13(c) compares the histograms of equivalent strains in the initial and optimised designs. The optimised scaffold achieved a lower standard deviation with a mean value of 1×10^{-3} in comparison with that of the initial design, indicating a notable uniform strain pattern achieved by the proposed method. Fig. 13(f) also compares the strain contours in the initial and optimal designs, further exhibiting the uniformity of the strain pattern.

Fig. 13(e) illustrates the distributions of optimised design variables and the details of non-uniform unit-cells. It can be observed that the side away from the bone fixation plate was reinforced with a large struct size; whereas the side nearby the bone fixation plate was structured with a smaller struct size to achieve an as-possible uniform strain pattern around the targeted value.

4. Discussion

ML methods have been extensively studied in design optimisation, particularly for the design of metamaterials with exotic behaviours [7–11]. Nevertheless, further investigations are required to explore design optimisation of lattice structures using artificial intelligence. The proposed DANN-based framework exhibits a notable advantage over conventional FE^2 optimisation approaches in terms of computational efficiency in design of non-uniform lattice structures. Although the same optimisation problems can also be performed by conventional FE^2 approaches, micro-FE analyses must be conducted on each unit-cell repeatedly, which will result in a prohibitively high computational burden. In contrast, by leveraging the DANN-based approach, one can directly undertake an optimal design solely with a macro finite element (FE) model, rendering the process more efficient than conventional FE^2 approaches. For example, in the case of the cantilever beam, the tests were also carried out by employing the conventional FE^2 approach on a desktop computer (CPU: Intel i7–7820X, RAM: 128 GB). For a single loop, the FE-based homogenisation and sensitivity analyses were

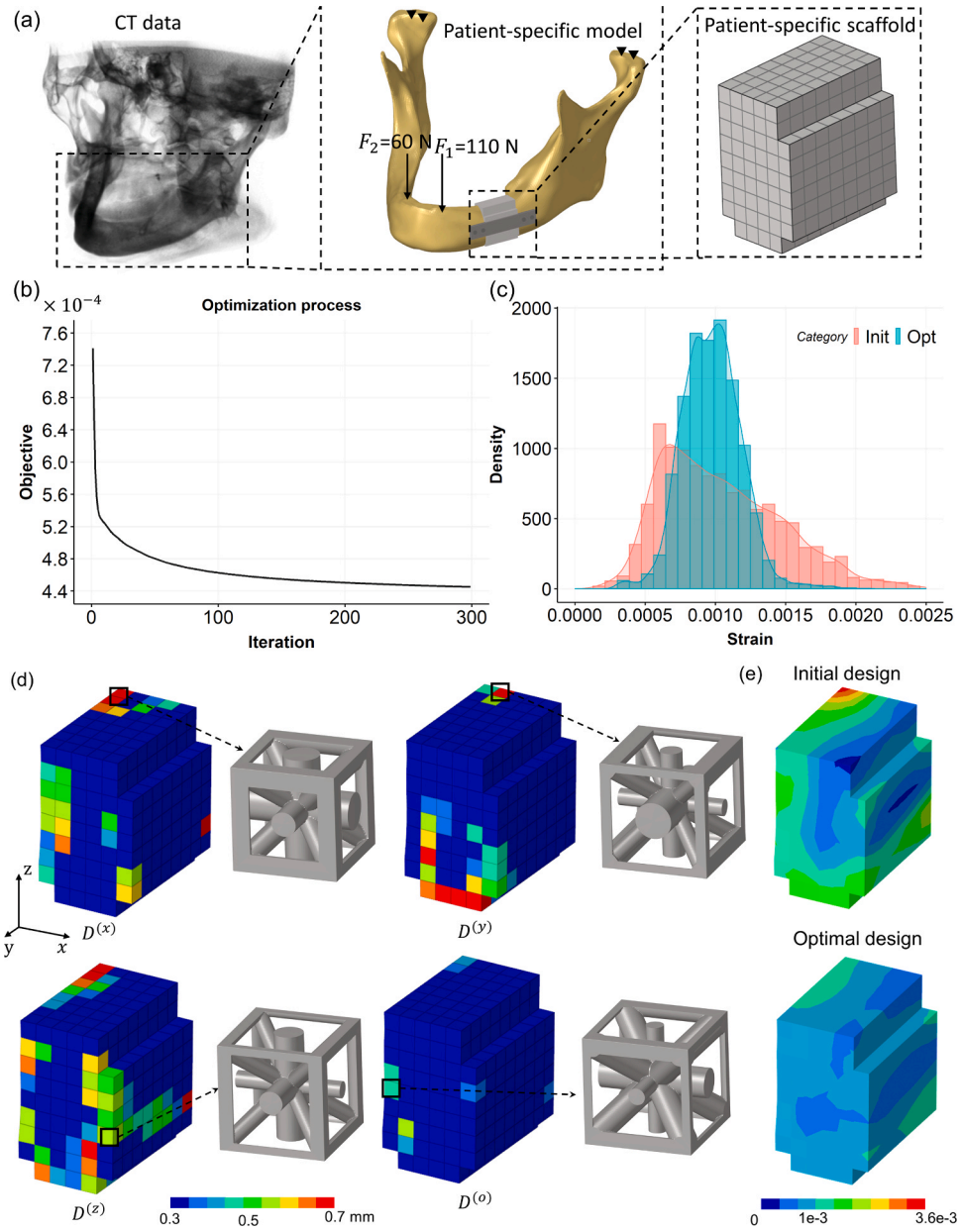

Fig. 12. A patient-specific design of the bone scaffold for mandibular reconstruction. (a) The patient-specific geometry model constructed from the CT data. The upper regions of the condyle are fully fixed, and the two point loads are applied to the front tooth region to simulate biting forces. The scaffold is meshed by 400 cubic elements with a size of 2 mm. (b) The iteration history of the objective function. (c) The histogram comparison of equivalent strains from the initial and optimal designs. (d) The distributions of the optimised design variables. (e) Comparison of equivalent strain contours in the initial and optimal designs.

performed on all 1764 lattice unit cells, necessitating a total of 2646 min. Furthermore, the macro-FE analysis and the adjoint FE analysis used for calculating macro sensitivity required an additional minute. If we adopted the conventional FE^2 approach for the design optimisation with 300 iterations, it could command a total of 794, 100 min (around 551 days), implying its impractice due to the prohibitive computational cost. Whereas in this study, the presented four cases (centre hole plate, cantilever beam, mandibular reconstruction, and femur bone reconstruction) only demanded 250, 300, 565, and 2380 min respectively, when utilizing the proposed method. These drastically reduced computational costs underline the superior efficiency of the proposed DANN-based approach.

The trained DANN models offer the advantage of reusability in design of non-uniform lattice structures, making them applicable across diverse engineering fields, including, but not limited to, aerospace, automotive, and mechanical engineering. Particularly, the DANN models allow to accommodate various emerging applications, such as design of non-uniform tissue scaffolds as well as various implantable medical devices, which promises significant benefits in personalised medicine with a potentially improved longevity of treatment outcome.

The FE-based homogenisation, as defined in Eq. (29), was developed for materials with linear elastic properties. In the situations where iso-truss lattices comprise materials with a constant Poisson's ratio (0.3 as used in this study) but varying Young's modulus values, the trained DANN can still be employed to predict their effective elastic tensors through a direct scaling procedure, thereby circumventing the necessity for additional training processes. Moreover, the dimensionless nature of the micro-FE models allows iso-truss lattices with different unit-cell sizes to directly benefit the trained DANN.

The proposed approach can be extended to consider other types of lattices as the base configuration. To achieve this, nevertheless, new ground-truth data using the geometric projection technique and FE-

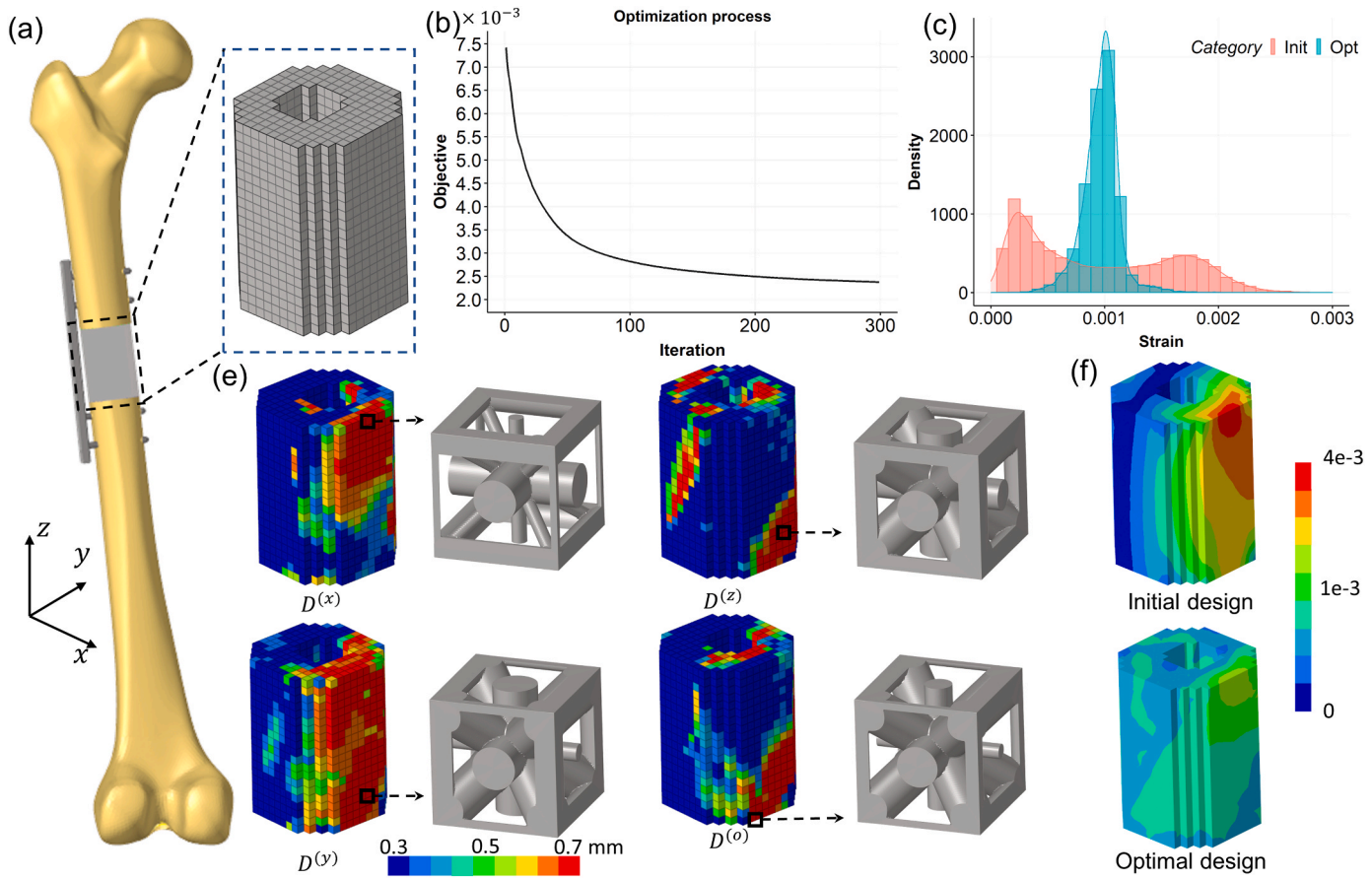

Fig. 13. The optimisation for a femur bone reconstruction case. (a) The bone-scaffold system includes a femur bone, a bone fixation plate, screws and a scaffold. (b) The iteration history of the objective function for scaffold design during the optimisation process. (c) The histogram comparison of the equivalent strains obtained from the initial and optimal designs. (e) The distributions of design variables in the optimised scaffold. (f) The comparison of the equivalent strain contours in the initial and optimal designs.

based homogenisation must be prepared for re-training the DANN models intended for the new base structural configuration. Even though, the same framework presented in this study can be utilised for design of other functionally graded lattice structures.

This study demonstrates two real-life bone reconstruction cases to optimise the bone scaffolds for biomedical applications. By determining the targeted strain level for a specific anatomy and defect site, the optimised design enables to achieve as-possible uniform strain, hypothetically leading to better bone regeneration outcomes with uniformly distributed bony tissue inside scaffolds. In addition, the proposed DANN-based optimisation framework is expected to apply to other orthopaedic devices, such as dental implants, hip implants, bone fixation plates, and spinal cages which are commonly of strong strain and stress shielding, preventing from a proper osseointegration and bone remodelling process.

Further studies can extend the proposed DANN optimisation framework to design of other lattice structures with a focus on better promoting bone growth in different mechanobiological contexts [54]. For example, stress, strain energy or their revised form have been widely employed as mechanical stimuli for bone formation in literature [13,55,56,61]. The proposed DANN framework can easily consider these stress or strain energy-related objectives by simply modifying the macro sensitivity analysis. Looking forward, the proposed DANN optimisation framework can be also extend into time/path-dependent design problems by considering the dynamic change of mechanical conditions in the course of bone regeneration.

Nevertheless, there are several issues that warrant further investigation. First, the optimised results exhibit non-smooth transitions in diameters between adjacent lattices. These uneven changes may give rise to heightened geometrical deviations between the as-designed and as-built samples due to the manufacturing limits, thereby enlarging the disparities between simulated and experimental outcomes [57]. One potential resolution lies in adoption of a density-based approach that has been employed in topology optimization methods [58,59]. Such an approach seeks to minimise variations in the design variables between neighbouring elements, consequently promoting smoother and more gradual transitions.

Second, a discernible disparity in strain patterns emerges when comparing the simulation results with those obtained through DIC tests in the presented cases. The intrinsic nature of PBF often induces residual stress, geometric deviations, and possible microcracks in the 3D fabricated specimens. Although we undertook heat treatment processes to mitigate residual stress, it is inevitable that certain geometrical deviations and microcracks might have persisted. These factors would likely contribute on the observed inconsistencies of the strain patterns obtained from the simulation and DIC tests.

Finally, it is essential to account for manufacturing uncertainties in the proposed approach for designing more robust additive-manufactured functionally graded lattice structures. By incorporating such uncertainties into the design process, a more comprehensive understanding of the potential deviations and discrepancies arising from the fabrication process can be obtained, thus aiding in the improvement of the overall design robustness [60].

5. Conclusions

This study developed a new optimisation framework for design of additively manufactured lattice structures by incorporating a derivative-aware neural network (DANN). The DANN enables to predict not only the homogenised material properties of unit-cells but also the sensitivity of the material properties with respect to design variables for topology optimisation. An as-possible uniform strain pattern with a prescribed magnitude can be achieved by efficiently tailoring the geometries of each single unit-cell. The two illustrative examples were first studied to validate the effectiveness of the proposed optimisation framework through the experimental tests on the 3D printed prototypes and digital image correlation (DIC) analysis. Following this, design of the two patient and/or site-specific bone scaffolds were further explored, which demonstrated considerable potential for real-world case scenarios. The proposed optimisation framework is expected to provide a computational tool for design of other porous structures in aerospace, biomedical, mechanical and civil engineering.

CRediT authorship contribution statement

Chi Wu: Conceptualization, Methodology, Software, Formal analysis, Investigation, Visualization, Visualization, Validation, Project administration, Methodology, Investigation, Formal analysis, Data curation, Conceptualization, Resources, Writing - original draft, Writing - review & editing. **Junjie Luo:** Validation, Formal analysis, Investigation, Visualization, Validation, Methodology, Writing - original draft, Writing - review & editing. **Jingxiao Zhong:** Resources, Methodology. **Yanan Xu:** Formal analysis, Resources. **Boyang Wan:** Validation, Methodology. **Wenwei Huang:** Resources. **Jianguang Fang:** Conceptualization, Supervision, Writing - review & editing. **Grant P. Steven:** Funding acquisition, Writing - review & editing. **Guangyong Sun:** Project administration, Funding acquisition, Resources, Writing - review & editing. **Qing Li:** Conceptualization, Supervision, Project administration, Funding acquisition, Supervision, Funding acquisition, Conceptualization, Investigation, Writing - review & editing.

Declaration of Competing Interest

The authors declare that they have no known competing financial interests or personal relationships that could have appeared to influence the work reported in this paper.

Data availability

Data will be made available on request.

Acknowledgements

We acknowledge financial support from the Australian Research Council (ARC) through the Discovery project (DP230103180). The Artemis HPC provided by the Sydney Informatics Hub, a Core Research Facility of the University of Sydney, is acknowledged.

References

[1] X. Yan, X. Huang, G. Sun, Y.M. Xie, Two-scale optimal design of structures with thermal insulation materials, Compos. Struct. 120 (2015) 358–365.
[2] E. Garner, J. Wu, A.A. Zadpoor, Multi-objective design optimization of 3D micro-architected implants, Comput. Methods Appl. Mech. Eng. 396 (2022).
[3] M. Xiao, X. Liu, Y. Zhang, L. Gao, J. Gao, S. Chu, Design of graded lattice sandwich structures by multiscale topology optimization, Comput. Methods Appl. Mech. Eng. 384 (2021), 113949.
[4] J. Plocher, A. Panesar, Effect of density and unit cell size grading on the stiffness and energy absorption of short fibre-reinforced functionally graded lattice structures, Addit. Manuf. 33 (2020), 101171.
[5] A. Panesar, M. Abdi, D. Hickman, I. Ashcroft, Strategies for functionally graded lattice structures derived using topology optimisation for additive manufacturing, Addit. Manuf. 19 (2018) 81–94.
[6] G. Allaire, R. Brizzi, A multiscale finite element method for numerical homogenization, Multiscale Model. Simul. 4 (3) (2005) 790–812.
[7] Z. Fang, J. Zhan, Deep physical informed neural networks for metamaterial design, IEEE Access 8 (2020) 24506–24513.
[8] L. Zhu, L. Sun, X. Wang, N. Li, Optimisation of three-dimensional hierarchical structures with tailored lattice metamaterial anisotropy, Mater. Des. 210 (2021).
[9] Y. Chang, H. Wang, Q. Dong, Machine learning-based inverse design of auxetic metamaterial with zero Poisson's ratio, Mater. Today Commun. 30 (2022).
[10] D.A. White, W.J. Arrighi, J. Kudo, S.E. Watts, Multiscale topology optimization using neural network surrogate models, Comput. Methods Appl. Mech. Eng. 346 (2019) 1118–1135.
[11] L. Wang, J. Boddapati, K. Liu, P. Zhu, C. Daraio, W. Chen, Mechanical cloak via data-driven aperiodic metamaterial design, Proc. Natl. Acad. Sci. 119 (13) (2022), e2122185119.
[12] J. Wang, A. Panesar, Machine learning based lattice generation method derived from topology optimisation, Addit. Manuf. 60 (2022), 103238.
[13] C. Wu, J.-G. Fang, A. Entezari, G.-Y. Sun, M.V. Swain, Y.-N. Xu, G.P. Steven, Q. Li, A time-dependent mechanobiology-based topology optimization to enhance bone growth in tissue scaffolds, J. Biomech. (2021).
[14] Y. Chen, S. Zhou, Q. Li, Microstructure design of biodegradable scaffold and its effect on tissue regeneration, Biomaterials 32 (22) (2011) 5003–5014.
[15] S. Sturm, S. Zhou, Y.W. Mai, Q. Li, On stiffness of scaffolds for bone tissue engineering-a numerical study, J. Biomech. 43 (9) (2010) 1738–1744.
[16] J.-H. Ahn, J. Kim, G. Han, D. Kim, K.-H. Cheon, H. Lee, H.-E. Kim, Y.-J. Kim, T.-S. Jang, H.-D. Jung, 3D-printed biodegradable composite scaffolds with significantly enhanced mechanical properties via the combination of binder jetting and capillary rise infiltration process, Addit. Manuf. 41 (2021).
[17] Y. Jin, S. Zou, B. Pan, G. Li, L. Shao, J. Du, Biomechanical properties of cylindrical and twisted triply periodic minimal surface scaffolds fabricated by laser powder bed fusion, Addit. Manuf. 56 (2022).
[18] W. Li, X. Cheng, Y. Wang, S. Wang, Projection printing of scaffolds with shape recovery capacity and simultaneously improved stiffness and toughness using an ultra-fast-curing poly(propylene fumarate)/hyperbranched additive resin, Addit. Manuf. 48 (2021).
[19] C.-S. Wu, S.-S. Wang, D.-Y. Wu, W.-L. Shih, Novel composite 3D-printed filament made from fish scale-derived hydroxyapatite, eggshell and polylactic acid via a fused fabrication approach, Addit. Manuf. 46 (2021).
[20] M. Zhang, C. Qin, Y. Wang, X. Hu, J. Ma, H. Zhuang, J. Xue, L. Wan, J. Chang, W. Zou, C. Wu, 3D printing of tree-like scaffolds for innervated bone regeneration, Addit. Manuf. 54 (2022).
[21] J. Plocher, A. Panesar, Review on design and structural optimisation in additive manufacturing: Towards next-generation lightweight structures, Mater. Des. 183 (2019), 108164.
[22] X. Wang, S. Xu, S. Zhou, W. Xu, M. Leary, P. Choong, M. Qian, M. Brandt, Y.M. Xie, Topological design and additive manufacturing of porous metals for bone scaffolds and orthopaedic implants: A review, Biomaterials 83 (2016) 127–141.
[23] J. Li, X. Cui, G.J. Hooper, K.S. Lim, T.B.F. Woodfield, Rational design, bio-functionalization and biological performance of hybrid additive manufactured titanium implants for orthopaedic applications: A review, J. Mech. Behav. Biomed. Mater. 105 (2020), 103671.
[24] M.P. Bendsøe, O. Sigmund, Material interpolation schemes in topology optimization, Arch. Appl. Mech. (Ing. Arch.) 69 (9–10) (1999) 635–654.
[25] G. Allaire, F. Jouve, A.-M. Toader, A level-set method for shape optimization, Comptes Rendus Math. 334 (12) (2002) 1125–1130.
[26] M.Y. Wang, X. Wang, D. Guo, A level set method for structural topology optimization, Comput. Methods Appl. Mech. Eng. 192 (1–2) (2003) 227–246.
[27] X. Huang, Y.M. Xie, Bi-directional evolutionary topology optimization of continuum structures with one or multiple materials, Comput. Mech. 43 (3) (2009) 393–401.
[28] D.-m XIAO, Y.-q YANG, X.-b SU, W. Di, Z.-y LUO, Topology optimization of microstructure and selective laser melting fabrication for metallic biomaterial scaffolds, Trans. Nonferrous Met. Soc. China 22 (10) (2012) 2554–2561.
[29] C. Lin, N. Kikuchi, S.J. Hollister, A generalized scaffold internal architecture design method using topology optimization, Summer bioengineering conference. Sonesta Beach Resort in Key Biscayne, Florida: June, 2003, pp. 25–29.
[30] M.R. Dias, J.M. Guedes, C.L. Flanagan, S.J. Hollister, P.R. Fernandes, Optimization of scaffold design for bone tissue engineering: A computational and experimental study, Med. Eng. Phys. 36 (4) (2014) 448–457.
[31] S.J. Hollister, C.Y. Lin, Computational design of tissue engineering scaffolds, Comput. Methods Appl. Mech. Eng. 196 (31–32) (2007) 2991–2998.
[32] V.J. Challis, A.P. Roberts, J.F. Grotowski, L.C. Zhang, T.B. Sercombe, Prototypes for bone implant scaffolds designed via topology optimization and manufactured by solid freeform fabrication, Adv. Eng. Mater. 12 (11) (2010) 1106–1110.
[33] C. Metz, G.N. Duda, S. Checa, Towards multi-dynamic mechano-biological optimization of 3D-printed scaffolds to foster bone regeneration, Acta Biomater. 101 (2020) 117–127.
[34] A.-M. Pobloth, S. Checa, H. Razi, A. Petersen, J.C. Weaver, K. Schmidt-Bleek, M. Windolf, A.Á. Tatai, C.P. Roth, K.-D. Schaser, G.N. Duda, P. Schwabe, Mechanobiologically optimized 3D titanium-mesh scaffolds enhance bone regeneration in critical segmental defects in sheep, Sci. Transl. Med. 10 (423) (2018).
[35] J.J. Li, C.R. Dunstan, A. Entezari, Q. Li, R. Steck, S. Saifzadeh, A. Sadeghpour, J. R. Field, A. Akey, M. Vielreicher, A novel bone substitute with high bioactivity, strength, and porosity for repairing large and load-bearing bone defects, Adv. Healthc. Mater. 8 (8) (2019), 1801298.

[36] H. Zhang, M. Song, M. Yang, Y. Song, F. Zhang, A. Zhang, L. Ruan, M. Wan, Fast Von Mises strain imaging on ultrasound carotid vessel wall by flow driven diffusion method, Australas. Phys. Eng. Sci. Med. 41 (2018) 669–686.
[37] R.L. Maurice, J. Ohayon, Y. Frétigny, M. Bertrand, G. Soulez, G. Cloutier, Noninvasive vascular elastography: Theoretical framework, IEEE Trans. Med. Imaging 23 (2) (2004) 164–180.
[38] J.A. Norato, B.K. Bell, D.A. Tortorelli, A geometry projection method for continuum-based topology optimization with discrete elements, Comput. Methods Appl. Mech. Eng. 293 (2015) 306–327.
[39] S. Watts, D.A. Tortorelli, A geometric projection method for designing three-dimensional open lattices with inverse homogenization, Int. J. Numer. Methods Eng. 112 (11) (2017) 1564–1588.
[40] J.F. Bourgat, Numerical experiments of the homogenization method. Lecture Notes in Mathematics, Springer Berlin Heidelberg,, 1979, pp. 330–356.
[41] L. Xia, P. Breitkopf, Design of materials using topology optimization and energy-based homogenization approach in Matlab, Struct. Multidiscip. Optim. 52 (6) (2015) 1229–1241.
[42] R. Hecht-Nielsen, Theory of the backpropagation neural network, Neural networks for perception, Elsevier (1992) 65–93.
[43] D.C. Liu, J. Nocedal, On the limited memory BFGS method for large scale optimization, Math. Program. 45 (1) (1989) 503–528.
[44] A. Florian, An efficient sampling scheme: updated latin hypercube sampling, Probabilistic Eng. Mech. 7 (2) (1992) 123–130.
[45] M.V. Narkhede, P.P. Bartakke, M.S. Sutaone, A review on weight initialization strategies for neural networks, Artif. Intell. Rev. 55 (1) (2022) 291–322.
[46] C. Zillober, A globally convergent version of the method of moving asymptotes, Struct. Optim. 6 (3) (1993) 166–174.
[47] R. Cintrón, V. Saouma, Strain measurements with the digital image correlation system Vic-2D, System 106 (2008) 2D.
[48] R. Ahmad, J. Chen, M.I. Abu-Hassan, Q. Li, M.V. Swain, Investigation of mucosa-induced residual ridge resorption under implant-retained overdentures and complete dentures in the mandible, Int. J. Oral. Maxillofac. Implants 30 (3) (2015).
[49] K. Zheng, N. Yoda, J. Chen, Z. Liao, J. Zhong, C. Wu, B. Wan, S. Koyama, K. Sasaki, C. Peck, Bone remodeling following mandibular reconstruction using fibula free flap, J. Biomech. 133 (2022), 110968.
[50] F.A. Schulte, D. Ruffoni, F.M. Lambers, D. Christen, D.J. Webster, G. Kuhn, R. Muller, Local mechanical stimuli regulate bone formation and resorption in mice at the tissue level, PLoS One 8 (4) (2013), e62172.
[51] C.H. Turner, M. Forwood, J.Y. Rho, T. Yoshikawa, Mechanical loading thresholds for lamellar and woven bone formation, J. Bone Miner. Res. 9 (1) (1994) 87–97.
[52] Y.F. Hsieh, A.G. Robling, W.T. Ambrosius, D.B. Burr, C.H. Turner, Mechanical loading of diaphyseal bone in vivo: the strain threshold for an osteogenic response varies with location, J. Bone Miner. Res. 16 (12) (2001) 2291–2297.
[53] D. Cullen, R. Smith, M. Akhter, Time course for bone formation with long-term external mechanical loading, J. Appl. Physiol. 88 (6) (2000) 1943–1948.
[54] L. Wang, J. Wang, Q. Chen, Q. Li, J.B. Mendieta, Z. Li, How getting twisted in scaffold design can promote bone regeneration: A fluid-structure interaction evaluation, J. Biomech. (2022), 111359.
[55] J. Sanz-Herrera, J. García-Aznar, M. Doblaré, On scaffold designing for bone regeneration: a computational multiscale approach, Acta Biomater. 5 (1) (2009) 219–229.
[56] R. Huiskes, W.V. Driel, P.J. Prendergast, K. Søballe, A biomechanical regulatory model for periprosthetic fibrous-tissue differentiation, J. Mater. Sci.: Mater. Med. 8 (12) (1997) 785–788.
[57] N. Korshunova, G. Alaimo, S.B. Hosseini, M. Carraturo, A. Reali, J. Niiranen, F. Auricchio, E. Rank, S. Kollmannsberger, Image-based numerical characterization and experimental validation of tensile behavior of octet-truss lattice structures, Addit. Manuf. 41 (2021), 101949.
[58] O. Sigmund, K. Maute, Topology optimization approaches: A comparative review, Struct. Multidiscip. Optim. 48 (6) (2013) 1031–1055.
[59] W. Wang, D. Feng, L. Yang, S. Li, C.C. Wang, Topology optimization of self-supporting lattice structure, Addit. Manuf. 67 (2023), 103507.
[60] A. Entezari, N.C. Liu, Z. Zhang, J. Fang, C. Wu, B. Wan, M. Swain, Q. Li, Nondeterministic multiobjective optimization of 3D printed ceramic tissue scaffolds, J. Mech. Behav. Biomed. Mater. 138 (2023), 105580.
[61] C. Wu, B. Wan, A. Entezari, J. Fang, Y. Xu, Q. Li, Machine Learning-Based Design for Additive Manufacturing in Biomedical Engineering, International Journal of Mechanical Sciences (2023) 108828.